KeAi
CHINESE ROOTS
GLOBAL IMPACT

Available online at www.keaipublishing.com/en/journals/journal-of-magnesium-and-alloys/

ScienceDirect

Journal of Magnesium and Alloys 20 (2026) 102094

www.elsevier.com/locate/jma

Full Length Article

Achieving high-strain-rate super-malleability of AZ31 alloy by ultrasonic vibration compression initiated at room temperature

Ziyue Xu[a,c], Huan Liu[a,b,*], Chao Sun[c], Luyao Li[c], Yuna Wu[a], Yue Zhang[d], Jinghua Jiang[a], Jing Bai[c], Yunchang Xin[e,**], Jiang Ma[f,**]

[a] College of Materials Science and Engineering, Hohai University, Changzhou 213200, China
[b] Suzhou Research Institute of Hohai University, Suzhou 215000, China
[c] College of Materials Science and Engineering, Southeast University, Nanjing 211189, China
[d] Institute of Metallic Biomaterials, Helmholtz-Zentrum Hereon, Geesthacht 21502, Germany
[e] Key Laboratory for Light-weight Materials, Nanjing Tech University, Nanjing 210009, China
[f] Shenzhen Key Laboratory of High Performance Nontraditional Manufacturing, College of Mechatronics and Control Engineering, Shenzhen University, Shenzhen 518060, China

Received 15 December 2025; received in revised form 26 March 2026; accepted 16 April 2026
Available online 15 May 2026

Abstract

Magnesium (Mg) alloy applications are severely limited by their poor room-temperature formability, which stems from the scarcity of thermally activated slip systems under ambient conditions. Here, we report a novel forming approach which can obtain exceptional malleability in an AZ31 Mg alloy sheet by ultrasonic vibration compression (UVC) initiated at room temperature. At a high strain rate of 3×10^{-1} s^{-1} and a low compression stress of 43.23 MPa, the 20 kHz UVC triggers significant deformation. This process achieves a true strain of 1.7 and a circumference expansion of 140%, demonstrating exceptional formability. This technique can be applied to prepare Mg products with various complex geometries including pentagram, square, hexagon, circle, and gear shapes. The high-frequency ultrasonic loading induces strong dislocation multiplication and entanglement that promotes the microstructure to evolve through three stages of (i) twinning-induced initial recrystallization, (ii) twin exhaustion followed by activation of non-basal slip systems, and (iii) shear band-mediated formation of ultrafine grains, ultimately achieving a considerable grain refinement. The microstructure evolution jointly supports the observed super compressive malleability. Our work provides a simple and effective approach to develop Mg alloy products at room temperature that has great industrial application value.

Keywords: Ultrasonic vibration; Magnesium alloy; Compression; Microstructure evolution; Malleability.

1. Introduction

As lightweight metallic structural alloys, Magnesium (Mg) and its alloys are highly regarded and possess significant potential for applications in aerospace, transportation, and communication industries owing to their superior specific strength and damping capacities [1–5]. However, Mg possesses a hexagonal close-packed structure with limited slip systems activatable at room temperature. Specifically, non-basal slip systems, including prismatic slip and <c + a> pyramidal slip, are difficult to activate [6–9]. Thus, Mg alloys usually exhibit poor ductility (cold formability) and are difficult to be deformed into components with complex shapes at room temperature [10,11]. This limitation severely restricts their widespread applications.

In recent decades, various strategies have been dedicated to enhancing the formability of Mg alloys. A primary strategy is

Peer review under the responsibility of Chongqing University
* Corresponding author at. College of Materials Science and Engineering, Hohai University, Changzhou 213200, China
** Corresponding authors.
E-mail addresses: liuhuanseu@hhu.edu.cn (H. Liu), ycxin@njtech.edu.cn (Y. Xin), majiang@szu.edu.cn (J. Ma).

https://doi.org/10.1016/j.jma.2026.102094

to activate non-basal slips by adding suitable elements to Mg alloys [12–14]. It is well established that the addition of calcium (Ca) or rare earth element (RE) can effectively improve the ductility of Mg alloys [15–17]. For example, Wang et al. [18] reported that a high ductility of 26.7% was achieved in the Mg-3Al-1Sn-0.5Ca-0.2Mn-0.1Sm alloy processed by high-temperature rolling. Similarly, a Mg-3Zn-1Gd hot rolled plate exhibited a value of 7.1 mm during Erichsen cupping tests [19]. The mechanism for this high ductility is mainly ascribed to two aspects, heightened non-basal slip activity and the formation of a weak texture. Another approach is to modify the strong basal texture of Mg sheets through plastic processing. Typical methods include equal channel angular pressing, differential speed rolling, asymmetric extrusion, side rolling to activate twinning [20–23]. He et al. [24] introduced a completely tilted basal texture with basal poles largely parallel to the TD in the AZ31 sheet through the pre-compression along the TD plus post annealing process. This tilted basal texture provides soft orientations for tensile twinning during the subsequent cold rolling process [25]. Jiang et al. [26] applied continuous variable cross-section direct extrusion to AZ31 alloy at 350 °C, which produced a weakened basal texture, resulting in a dramatically improved ductility.

Superplastic forming offers a potential means of forming wrought Mg alloys into complex shapes and overcoming their formability restrictions [27–28]. Grain size is considered an important parameter for achieving superplasticity in Mg alloys. Consequently, severe plastic deformation techniques, including equal channel angular pressing, friction stir processing, are effective methods for producing ultrafine grains with superplastic properties. Wu et al. added Ag to a Mg-Y-Er-Zn alloy, refined the grain size, and achieved 495% elongation at 623 K and a strain rate of 10^{-2} s^{-1} [29]. However, superplasticity behavior of Mg alloys is usually characterized by tensile tests, while industrial forming methods, such as stamping and drawing, are more closely associated with compression. As Lin et al. [30] reported, the temperature must be increased to at least 573 K for Mg alloys to achieve compressive superplasticity (characterized by a true strain reached 1.3; malleability). Under practical applications, elevated temperature can cause mold damage and reduce service life. So far, no reliable method is available for achieving room temperature forming of Mg alloys.

In recent years, ultrasonic vibration (UV) technology has been widely integrated into advanced manufacturing processes [31–33]. Based on the processing state, current UV applications in Mg alloys can be categorized into three domains: (i) liquid-phase processing (e.g., ultrasonic melt treatment) for grain refinement [34] (ii) ultrasonic welding for joining [35]; and (iii) solid-phase ultrasonic vibration-assisted (UV-A) forming. In solid-phase processes such as UV-A hot embossing [36], UV-A extrusion [37], and UV-A wire drawing [38], ultrasonic vibration is typically employed as an auxiliary energy field, applied intermittently or continuously to the punch. By facilitating dislocation slipping and reducing lattice resistance through the “acoustic softening” effect, these vibrations effectively lower the material’s flow stress and interfacial friction, thereby reducing the overall forming force [39,40].

Recent studies by Ma et al.’s group have pioneered a transformative approach utilizing ultrasonic vibration as the primary energy source to drive massive plastic deformation [41–43]. This technique, referred to as ultrasonic vibration compression (UVC) or ’’ultrasonic hammering,’’ exploits the high-frequency mechanical energy to significantly alter the thermodynamic and kinetic states of materials. Pioneering work by Ma et al. demonstrated that this energy-driving mode can induce localized structural rejuvenation and superplasticity in metallic glasses, enabling efficient shape forming at low macroscopic stresses [44]. Beyond non-crystalline systems, Zhang et al. [45] further extended UVC to the rapid forming of high-entropy alloys (HEAs) even under extreme cryogenic conditions (77 K), effectively overcoming the intrinsic low-temperature brittleness of metallic materials through high-frequency oscillatory stress fields. Unlike UV-A, UVC utilizes high-frequency vibration as the primary energy source and the direct driving force for plastic formation, requiring only minimal static loads to maintain acoustic coupling. More significantly, UVC transcends the surface constraints of conventional processes by directly injecting high-frequency vibrational energy into the material’s interior. This deep penetration triggers an instantaneous acoustic-thermal coupling that maximizes the “volume effect,” thus changing the intrinsic workability of an alloy from within.

Inspired by these advances in amorphous materials, we have successfully adapted this high-frequency impact concept to crystalline materials. Through UVC, we achieved superplastic forming in a commercially available AZ31 Mg plate, reaching a true strain of 1.7 and a circumference expansion of 140%. This UVC technology demonstrates exceptional versatility in fabricating components with complex geometries at room temperatures. This study systematically characterizes the microstructural evolution and deformation kinematics under the high-frequency ultrasonic field, elucidating the underlying mechanisms, particularly the synergy between acoustic-thermal coupling and localized dynamic recrystallization (DRX) that enables this deformation.

2. Experimental procedure

2.1. Materials

To evaluate the formability of Mg alloys under ultrasonic vibration compression (UVC), the commercially available AZ31 Mg alloy sheet was used as the starting material. The as-received AZ31 sheets, with a thickness of 3 mm and a width of 600 mm were purchased from Chongqing Yuhua New Material Technology Co., Ltd. The resulting sample was designated as the “as-received” sample. As shown in Fig. 1 the as-received AZ31 sheet has a fully recrystallized microstructure with an average grain size of approximately 13 μm. Regarding texture, the {0001} pole figure reveals a characteristic non-basal orientation where the basal poles are

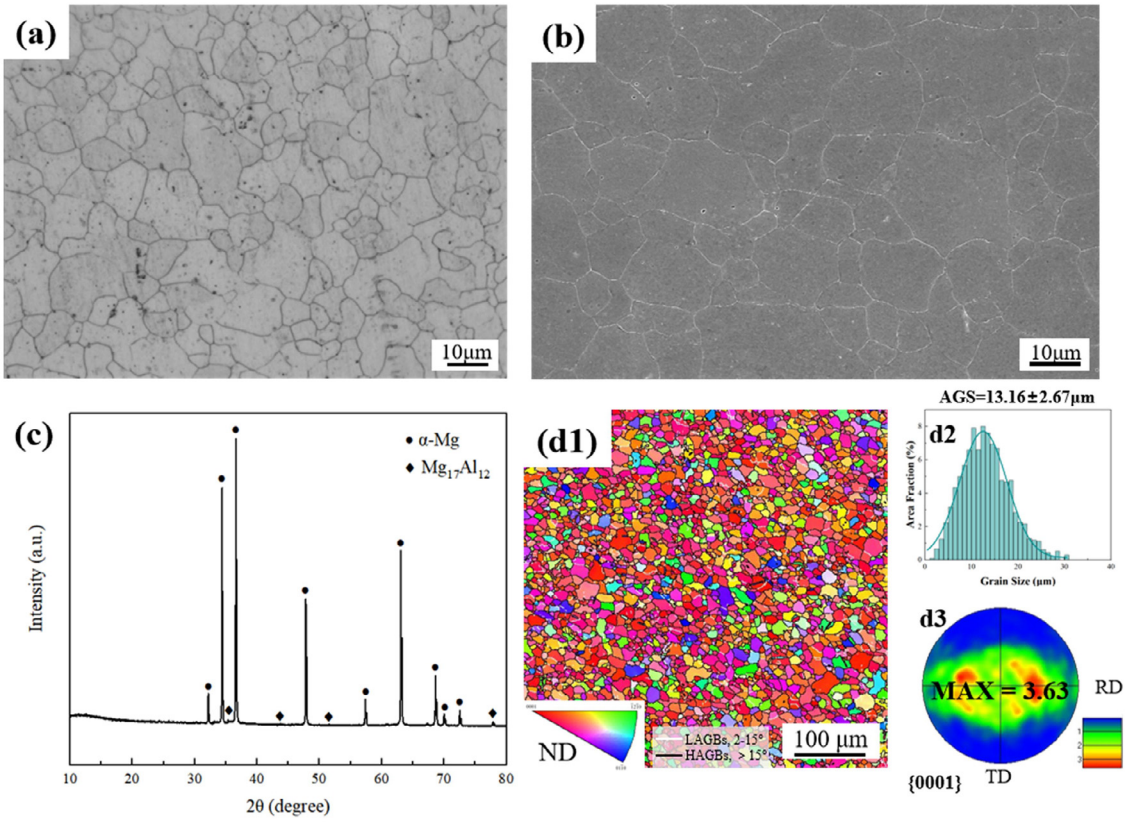

Fig. 1. Microstructure of initial as-received AZ31 alloy. (a) OM image, (b) SEM image, (c) XRD patterns, (d1) inverse pole figure (IPF) map, (d2) statistical grain size distribution and (d3) {0001} pole figure.

tilted about 40° away from ND toward RD. The maximum texture intensity of the sample is 3.28.

2.2. Ultrasonic vibration compression process

UVC tests were carried out using an ultrasonic plastic welding machine system (Shenzhen Hongri Ultrasonic Equipment Co., Ltd.). As illustrated in the schematic (Fig. 2a), the apparatus comprises four key components: an ultrasonic generator, a transducer, a booster, and a sonotrode. Operationally, the generator emits a 20 kHz electrical signal, which is subsequently transformed into high-frequency mechanical vibration by the transducer. These vibrations are then amplified and applied to the specimens through a sonotrode operating at an amplitude of 44.4 μm. The frequency and amplitude were selected following the work of Ma et al. [46,47]. Cylindrical specimens, measuring $\varphi 2 \times 2$ mm, were cut from the AZ31 sheet along the ND direction. The contacting end surfaces of all specimens were mechanically ground with 800–2000 grit SiC papers. No lubricant or any other surface coating was applied, thereby ensuring consistent dry-contact frictional conditions and direct acoustic coupling throughout the UVC process. The UVC processing consisted of three steps: First, the sample was fixed on the equipment platform. Second, the parameters were configured on the control panel. Finally, the ultrasonic vibration was initiated, and the sample was deformed under the downward pressure of the punch within seconds. More details about UVC processing can be found elsewhere [48,49].

To further evaluate the degree of deformation during the ultrasonic process, the following parameters (Eqs. (1) and (2)) were used:

$$\varepsilon_T = \ln \frac{h}{h_0} \tag{1}$$

Where ε_T is the compressive true strain; h_0 is the height of the sample before deformation; h is the height of the sample after deformation.

$$CE = \frac{d - d_0}{d_0} \times 100\% \tag{2}$$

Where CE is the circumference elongation of the sample; d_0 is the diameter of the sample before UVC deformation; d is the diameter of the sample after UVC deformation. CE is the definition standard of realizing compression superplasticity of material [30]. A higher CE value indicates a greater capacity of the material to undergo large plastic deformation without fracturing, meaning CE and malleability are positively correlated. To enable real-time measurement of force during UVC, a pressure test platform was installed beneath the test platform, and a delicated data acquisition card (National Instruments NI-9237) was used for collecting the real-time pressure data. The sampling frequency of the pressure data was set at 500 Hz. Consequently, stress and time curves can be analyzed during the UVC process. Moreover, the infrared thermal

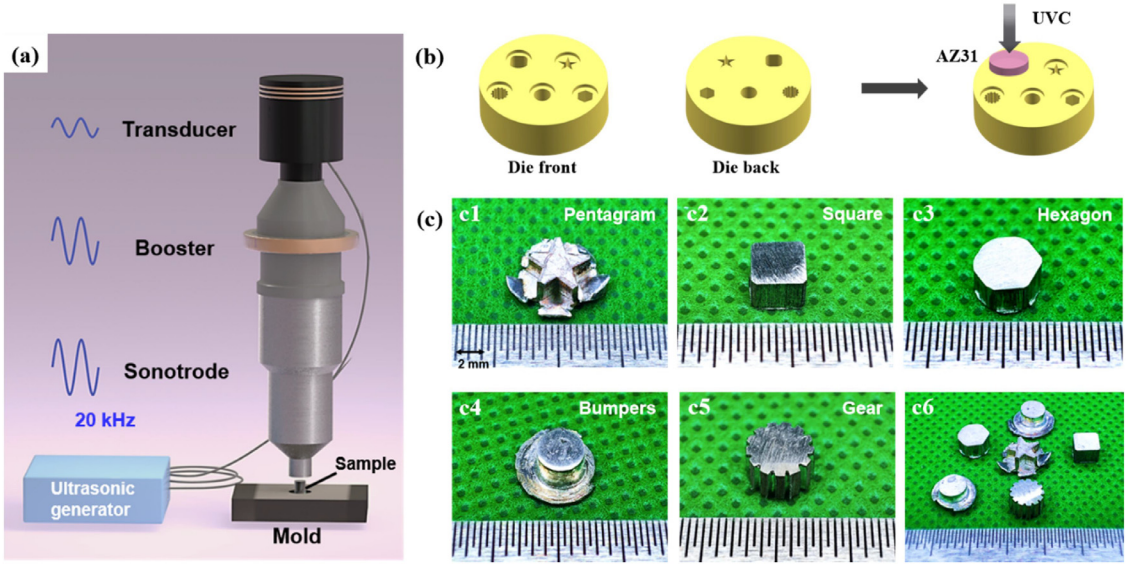

Fig. 2. Schematic diagrams of ultrasonic equipment and processes: (a) ultrasonic vibration compression process equipment; (b) macro-scale forming schematic diagram; (c) different complex forming types under ultrasonic vibrations. (c1) Pentagram. (c2) Square; (c3) Hexagon; (c4) Bumper; (c5) Gear; (c6) All macro-formed parts.

imaging thermograph (Fotric 280d) was used for temperature characterization to capture the temperature change trend and obtain specific temperature distributions at different locations during the UVC process.

To explore the feasibility of ultrasonic vibration compression forming (UVCF) for AZ31 alloy, a relevant mold and molding process were designed, as shown in Fig. 2b. The macro-scale forming mold incorporates templates including pentagram, square, hexagon, circle, and gear profiles as shaping dies. Cylindrical billets ($\varphi 5 \times 3$ mm) were positioned onto these dies, successfully producing components with complex micro-geometries. For comparative analysis, identical specimens underwent conventional compression (designated as "CC" sample). The displacement rate was set to 15 mm/min to match the effective strain rate of the UVC process.

2.3. Microstructure characterization

Cross-section of ultrasonic specimens was prepared for microscopic characterization. Phase constitution of the as-received alloy sheet was analyzed by a D8 DISCOVER X-ray diffractometer (XRD). An Olympus BHM optical metallographic microscope (OM) and a Sirion field-emission scanning electron microscope (SEM) fitted with a GENESIS 60S X-ray energy spectrometer (EDS) and electronic backscatter diffraction (EBSD) were employed to track the microstructure evolution. The OM and SEM specimens were mechanically ground by 180–2000 SiC papers, polished by 2.5 μm diamond spray. The microstructure was revealed using an etchant mixture of acetic acid, oxalic acid, and nitric acid (1 mL each) diluted in 150 mL of distilled water, concluding with an alcohol rinse. For EBSD, surface quality was ensured via electropolishing in 10% perchloric acid-ethanol solution at −40 °C. A constant step size of 0.3 μm was maintained during scanning to capture sufficient data points per grain. Post-data acquisition, including the assessment of grain size statistics and texture development, was executed using Aztec crystal software.

Furthermore, to elucidate the deformation mechanisms occurring inside the non-indexed zones, transmission Kikuchi diffraction (TKD) was conducted to achieve high-spatial-resolution characterization. Fine-scale microstructural observations were conducted using a Techni G2 transmission electron microscope (TEM). TEM specimens were ground to a thickness of 70–100 μm and electro-thinned at 4 kV for 10 min. For dislocation analysis, specimens were characterized using high-resolution TEM (HR-TEM, JEOL 2100F). Cross-sectional TEM samples were fabricated using focused ion beam (FIB) milling.

3. Results

3.1. Ultrasonic vibration compressive deformation behavior

Deformation behavior of AZ31 Mg alloy under CC and UVC at room temperature is shown in Fig. 3. Fig. 3a shows the stress-time curves during UVC process, revealing extremely low flow strength (peak value: 43.23 MPa) and a high strain rate of 3×10^{-1} s^{-1}. Fig. 3b contrasts CE and ε_T evolution at different processing times. UVC achieved $\varepsilon_T = 1.7$ and 140% CE, while CC reached only $\varepsilon_T = 0.6$. Fig. 3c compares macro-morphologies of as-received, CC, and UVC samples. After 1.5 s of UVC, cylindrical specimens compressed from height of 2 mm to 0.4 mm underwent no fracture, whereas CC samples fractured at 1.1 mm height.

For conciseness, UVC samples at characteristic deformation stages (true strains of 0.2, 0.6, 1.0, and 1.5) are des-

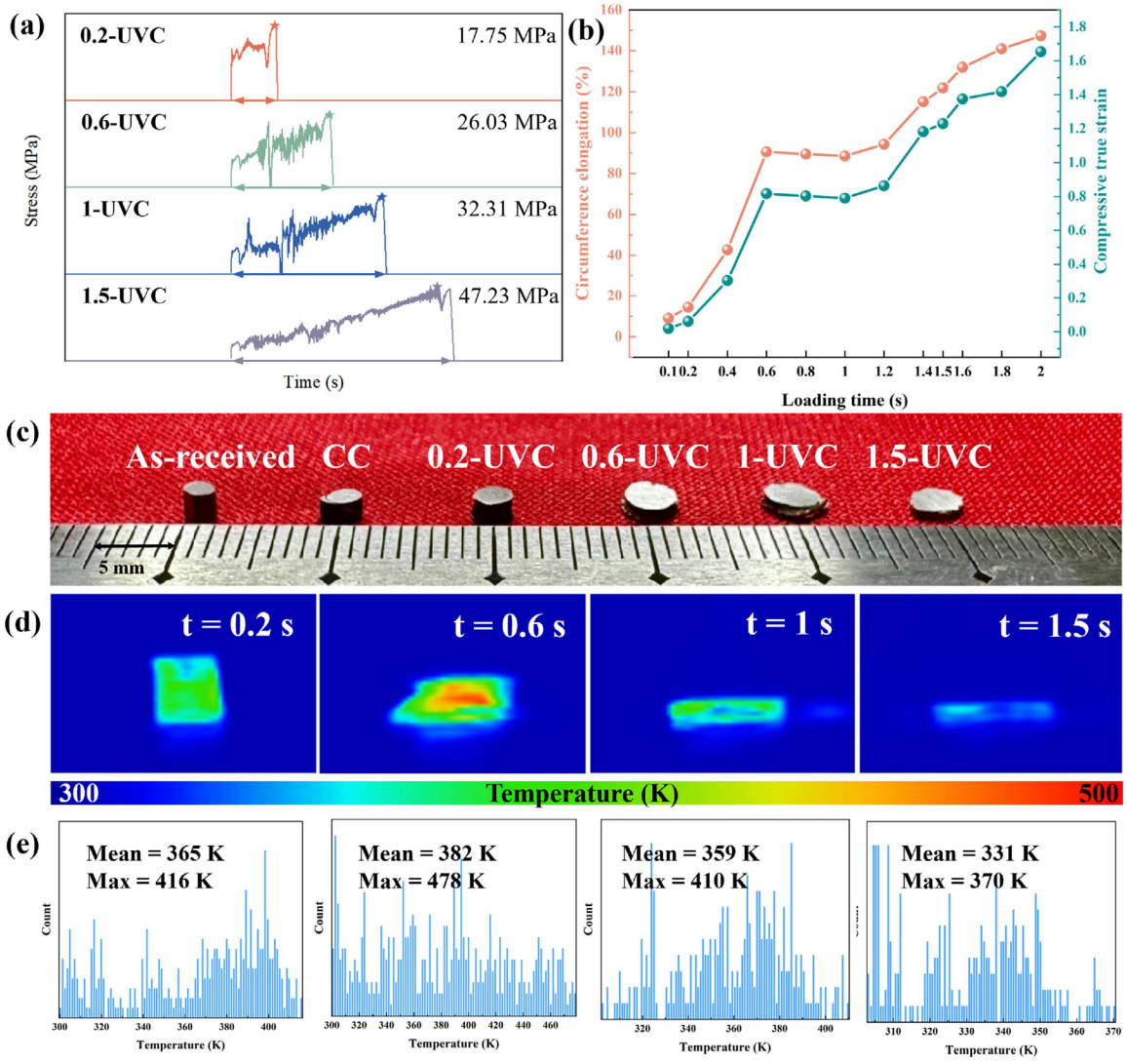

Fig. 3. Deformation behavior under different loading time after UVC. (a) Mechanical response of stress-time curve; (b) comparison of the circumference elongation (CE) and compressive strain (ε_T) after different loading time; (c) macroscopic deformation behaviors of the CC and UVC samples; (d) thermal infrared images of deformation area and (e) corresponding temperature numerical distribution of 0.2 s, 0.6 s, 1 s and 1.5 s.

ignated 0.2-UVC, 0.6-UVC, 1.0-UVC, and 1.5-UVC. Notably, despite a large deformation amount of 80%, no apparent cracks are detected on the surface of the UVC sample. Infrared thermography recorded temperature evolution during maximum deformation (Fig. 3d and 3e), showing rapid heating to ~478 K followed by rapid cooling. This temperature spike originates from UVC-induced energy dissipation as heat, compounded by adiabatic heating at a high strain rate (3×10^{-1} s^{-1}). Subsequent rapid cooling is attributed to high thermal conductivity and small specimen dimensions of AZ31 alloy. These distinct compression behaviors of the AZ31 alloy point to different deformation mechanisms under CC and UVC, which will be discussed in detail in the subsequent sections.

Based on the deformation behaviors of the AZ31 alloy mentioned above, the UVC process was applied to form various complex geometric shapes under ambient conditions. As shown in Fig. 2c1, pentagram structures were successfully formed with edge thickness below 0.1 mm without fracture. Fig. 2c2 shows the square-shaped component, while Fig. 2c3–c5 shows the hexagonal, bumper, and gear profiles, respectively. All formed features exhibit clean edges and precise geometries, with complete forming achieved within 2 s via ultrasonic vibration. Evidently, this UVC approach enables room-temperature forming of Mg alloy components with various complex geometries.

3.2. Microstructure evolution of AZ31 alloy during UVC

Fig. 4 shows the SEM images of UVC-AZ31 alloys. Under low strain UVC, grains exhibit minor elongation along the deformation axis (Fig. 4a and b). With increasing deformation (Fig. 4c), coarse grains are refined and deformation becomes inhomogeneous. In addition, shear bands distributed in a vertical direction of compression are observed. After large deformation (Fig. 4d), shear band zones form with zonal grain

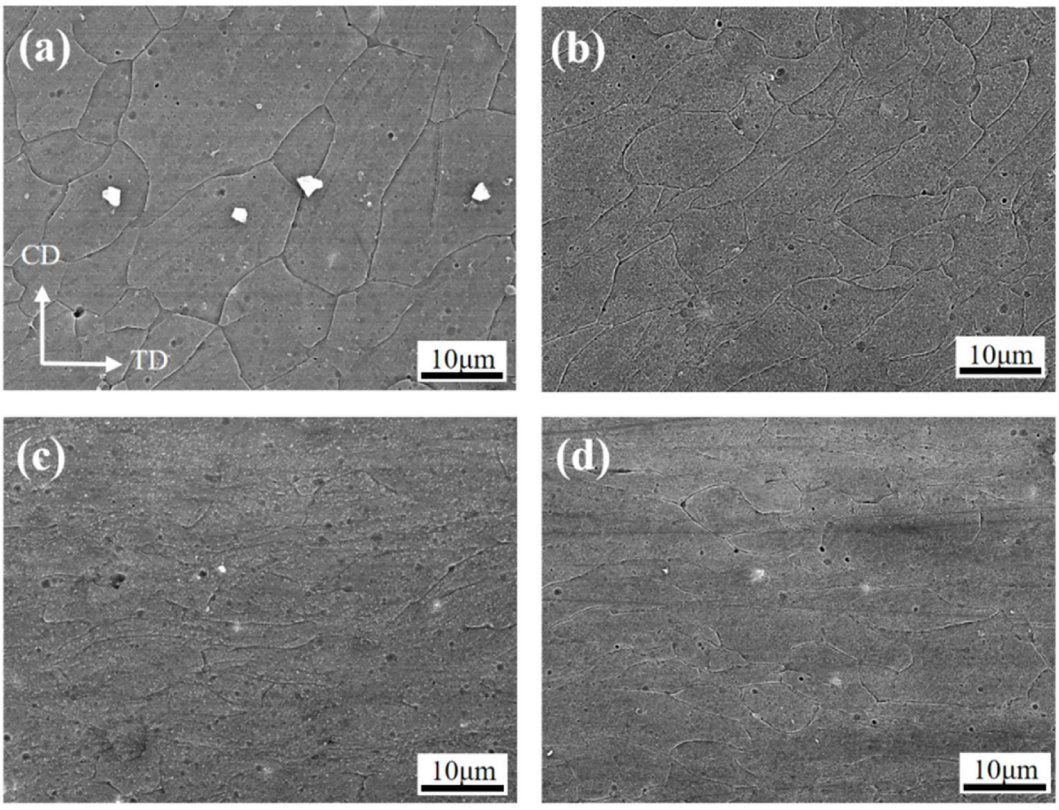

Fig. 4. SEM micrographs of UVC-AZ31 alloy. (a) 0.2-UVC, (b) 0.6-UVC, (c) 1-UVC, (d) 1.5-UVC.

distribution. These results show that the shear band may play an important role during UVC of AZ31 alloy sheet.

Fig. 5 shows the EBSD results of the UVC-AZ31 alloy after different strains. The evolution of the microstructure is shown by the inverse pole figure (IPF) maps (Fig. 5a1–e1). It can be seen that the grains before deformation show a random distribution, and the original grain size is about 7 μm (Fig. 5a2). Upon dynamic UVC loading, significant grain refinement occurs, generating a population of deformed grains that are elongated perpendicular to the compression direction (CD). Fig. 5a2–e2 depict the grain size distributions, revealing a typical bimodal structure for all samples [50]. For the 1.5-UVC alloy, coarse grains along the transverse direction are significantly elongated, and the average grain size is refined to 1.62 μm (Fig. 5e2). It should be noted that the black areas in the IPF maps correspond to zero resolution points caused by high residual stress after deformation. The emergence of clustered striped black bands around large grains is attributed to the severe lattice distortion during deformation and the resulting aggregation of finer grains [51]. Furthermore, most refined grains are preferentially clustered along shear bands and deformed grain boundaries. As shown in the {0001} poles figures, all samples exhibit a typical <0001>//CD compression texture [52]. Before deformation, a fiber texture with basal poles tilted about 40° away from CD towards TD is observed, exhibiting a maximum pole intensity of 21.36. With increasing UVC strain, an evident variation in texture is observed. The texture of the UVC alloy gradually aggregates toward the CD direction, with pole density concentrated at the CD pole. The UVC promotes a reduction in the texture intensity compared with the initial texture of the as-received alloy. The final texture with a strength of 13.47 is formed in the 1.5-UVC alloy (Fig. 5e3).

In order to further analyze the deformation mechanisms and reveal the formation process of shear bands, TEM micrographs (Fig. 6) of AZ31 during the UVC process were analyzed. A microstructure evolution from low strain to high strain was observed. Due to the input of ultrasonic energy, dislocation density is high, and dynamic recovery is prone to occur during dislocation sliding and climbing [53]. Dislocation entanglement forms low-angle grain boundaries (LAGBs), which consist primarily of sub-grains in Fig. 6a–b, and the average sub-grain size is about 782.5 nm (Fig. 6c). With increasing strain, the selected area electron diffraction (SAED) in Fig. 6d reveals that the 1.5-UVC alloy exhibits a complete dynamic recrystallized microstructure with a grain size of 461.1 nm. Focusing on the localized shear band zones (Fig. 6g–k), the 0.6-UVC alloy exhibits narrow and parallel band structures (Fig. 6g). Within these specific regions, tangled dislocations are still highly visible, a feature explicitly marked by the yellow arrows in Fig. 6h [54]. Fig. 6i and k show the morphologies of shear bands in the 1.5-UVC alloy, which still maintains a high density of dislocations. Dislocation slip promotes DRX around and inside shear band domains, leading to the formation of submicron grains inside the shear bands [55].

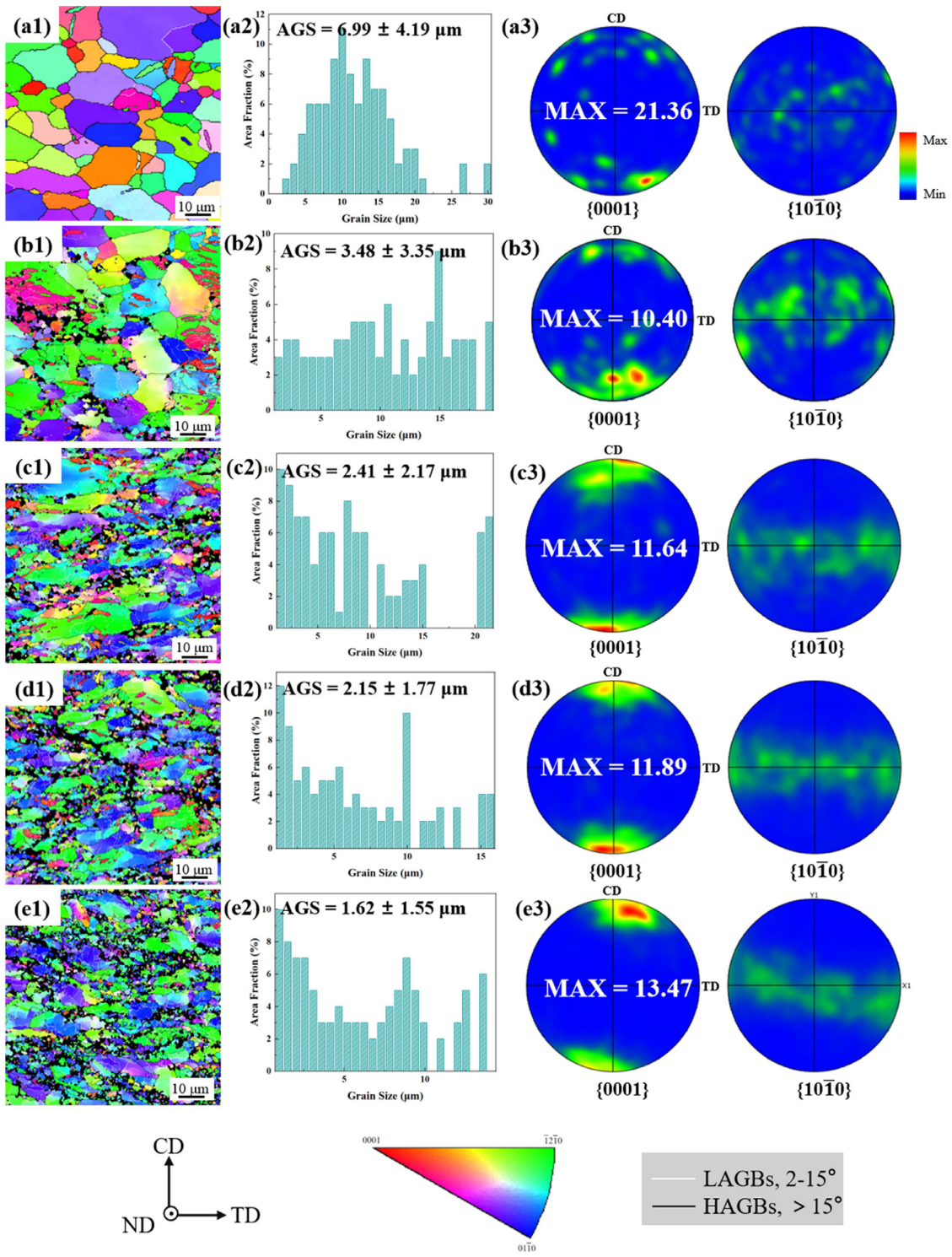

Fig. 5. IPF maps (a1–e1), grain size distributions (a2–e2) and {0001} and {10-10} pole figures (a3–e3) of UVC-AZ31 alloy in different deformation states. (a1–a3) As-received sample along RD direction, (b1–b3) 0.2-UVC alloy, (c1–c3) 0.6-UVC alloy, (d1–d3) 1-UVC alloy, (e1–e3) 1.5-UVC alloy.

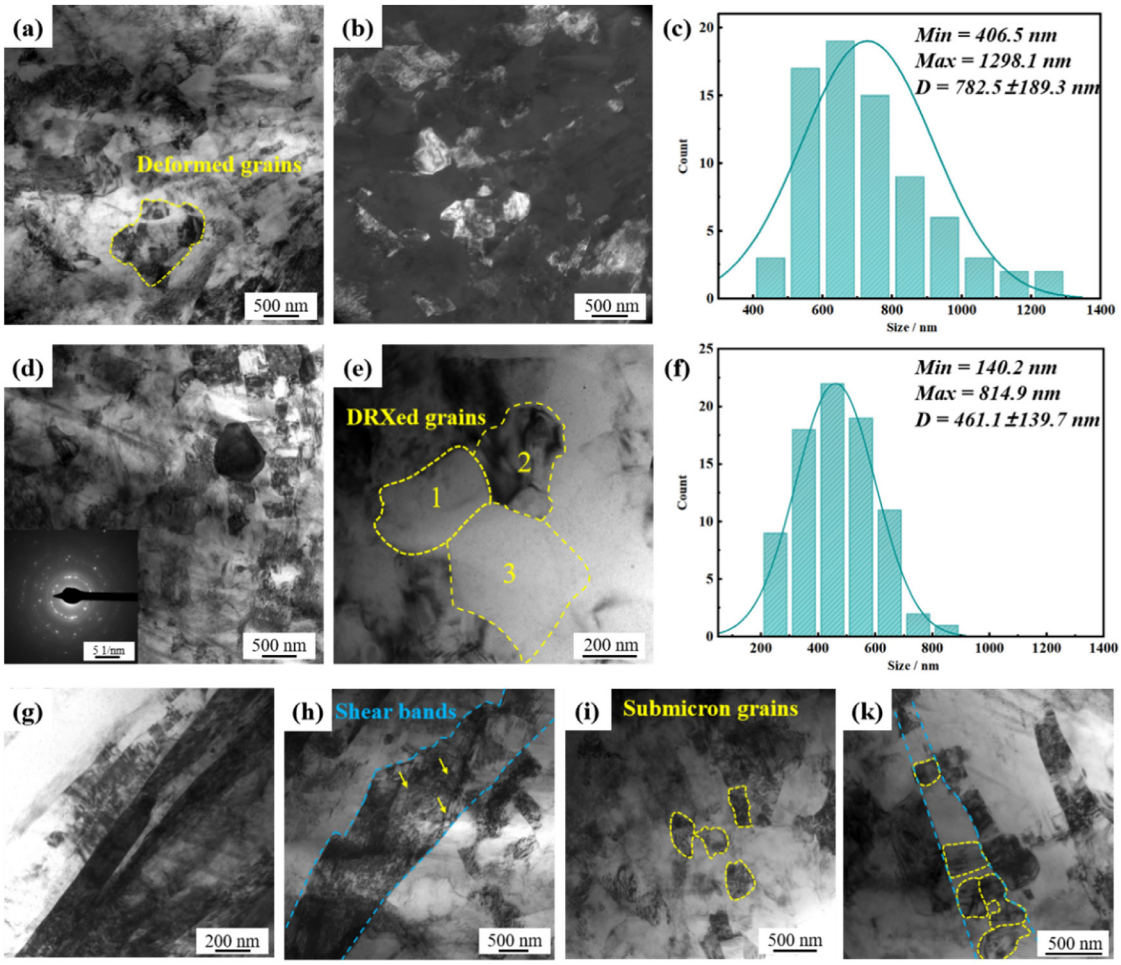

Fig. 6. TEM micrographs of UVC-AZ31 alloy: (a)–(b), (g)–(h) 0.6-UVC alloy; (d)–(e), (i)-(k) 1.5-UVC alloy; Grain size distributions of (c) 0.6-UVC and (f) 1.5-UVC alloy.

4. Discussions

4.1. Compression behavior of conventional loading of Mg alloys

Fig. 7 illustrates the deformation metrics comparison of the current UVC process and conventional compression for reported Mg-based alloys (Table S1). Here, compressive malleability is quantitatively reflected by the limiting true strain and CE that the material can sustain prior to fracture. Due to the high recrystallization temperature and limited slip systems, it is difficult to reach high true strain for Mg alloys at room temperature. This limitation is evidenced in Fig. 7, which shows that most conventional loading tests were carried out at elevated temperature or low strain rate, and few Mg alloys exceeded the true stain of 1.3, while the UVC process enables the AZ31 alloy sheet to achieve an exceptional true strain of 1.7 at a much higher strain rate of 0.3 s^{-1} under ambient conditions with no additional external heating. This result demonstrates that UVC endows the alloy with supermalleability, effectively overcoming the traditional trade-off between high strain rate and large deformation capacity.

4.2. The deformation mechanisms of AZ31 alloy sheet under UVC

4.2.1. Twinning evolution and initial deformation coordination

Fig. 8 shows the low-angle grain boundaries (LAGBs) and high-angle grain boundaries (HAGBs) distributions in all samples. Generally, misorientations of 2°−15° are considered as LAGBs, while misorientations >15° are regarded as HAGBs [56]. As shown in Fig. 8a, HAGBs predominate in the as-received alloy and contain a large number of twins, likely originating from twin accumulation during rolling and annealing. The concentrated distribution of 86° ± 5° (highlighted with blue background) corresponds to {10–12}<10−11> extension twin boundaries. For the 0.2-UVC alloy (Fig. 8b), insufficient slip system activation at a low deformation temperature promotes twin activation to accommodate deformation, resulting in an increase in twin boundary fraction to 32%. The ultrasonic energy causes a sharp increase in temperature, which further promotes twinning [57]. It was reported that sub-grain boundaries, deformation twins and shear bands were considered as the main nucleation sites for recrystallisation in

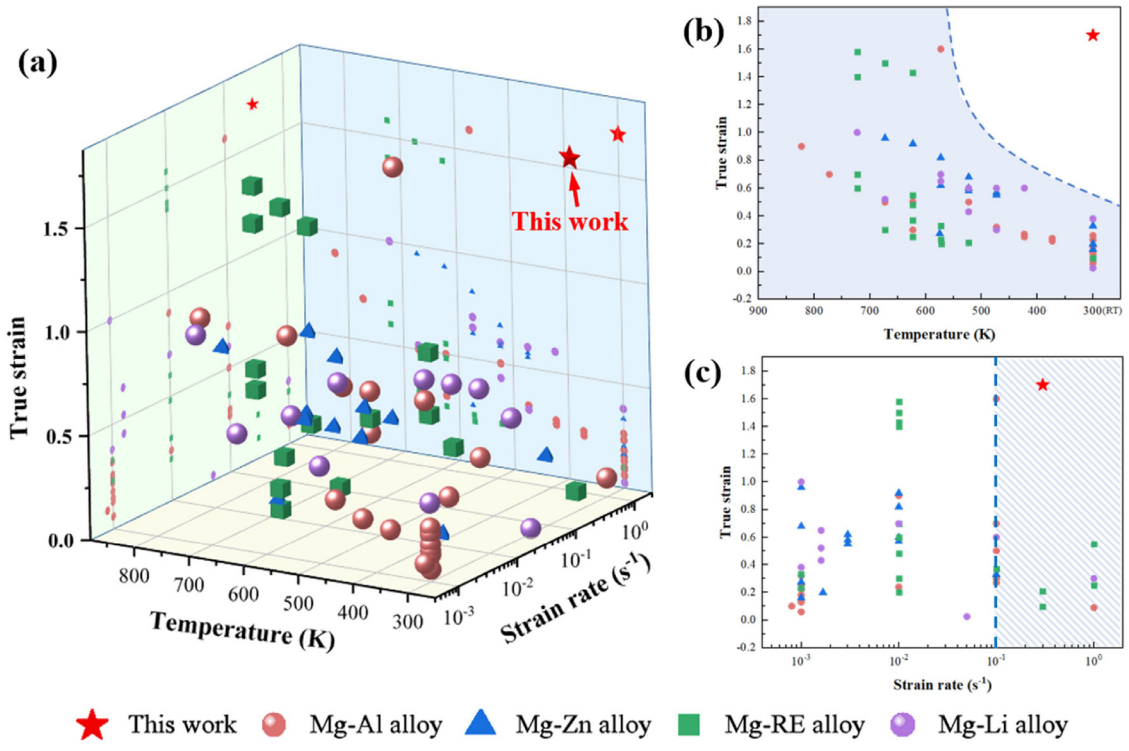

Fig. 7. Comparative assessment of deformation capabilities between UVC process and conventional compression for Mg-based alloys. (a) Multi-dimensional comparison of the temperature, strain rate, and true strain, (b) corresponding relationship between the temperature and true strain, (c) corresponding relationship between the strain rate and true strain.

Mg alloys [58,59]. In this work, recrystallization nucleation occurs at the twin boundaries and shear bands, consuming the initial twin with increased UVC processing [60]. After 1.5 s deformation, the microstructure becomes virtually devoid of twins (Fig. 5e1). Concurrently, the intensity of the [−12–10] axis distribution for 86° ± 5° peak in HAGBs progressively diminishes. Fig. 8f shows the variation trend of the twin boundary fraction with deformation time. The results reveal that the correlation of twin content on deformation time (namely true strain) is non-monotonic. Specifically, as deformation accumulates, the fraction of twins exhibits an initial surge followed by subsequent decline.

Moreover, twin generation could induce DRX, which facilitates fast deformation under UVC. Fig. 9 shows twin-induced DRX nucleation behavior in 0.2-UVC and 0.6-UVC alloys, with EBSD orientation maps extracted from amplified regions of Fig. 5. As shown in Fig. 9a, the original parent grains (P1, P2) contain twins (T1, T2). Combined with the grain boundaries map in Fig. 8, these are identified as $\{10\bar{1}2\}$ 86° ± 5° extension twin boundaries. Apparently, the fine DRX grain (e.g., D1) is observed around the twin. Similarly, Fig. 9b shows refined DRX grains (D1–D2) nucleating at twin interfaces with similar orientations—characteristic of continuous dynamic recrystallization (CDRX) [61,62]. Moreover, several sub-grains (S1–S13) are also formed in the vicinity of parent grain boundaries. At this small strain, sub-grains represent early stage DRX where parent grains are partially surrounded by DRX grains, while sub-grains dominate and recrystallization remains incomplete. With the aggravation of deformation, LAGBs transform into HAGBs through lattice rotation, evolving these sub-grains into DRX grains [63]. As shown in Fig. 9c–d, the parent grains are oriented along the direction of CD in the {0001} plane, while the formed DRX grains maintain twin-related orientations. Fig. 9e–f shows the point-to-point and point-to-region misorientation differences of the line inside the grains. The orientation difference between the points in the parent grain and the starting point is large (>10°), indicating a strong distortion in the parent grains. The accumulation of dislocations forms a large number of sub-grains, which are expected to develop into new DRX grains.

These observations collectively demonstrate twinning-assisted DRX as a dominant mechanism under the earlier stage of UVC [64]. The high-frequency ultrasonic vibration promotes profuse {10–12} extension twinning and localized high stored energy in shear bands, which serve as preferential sites for rapid nucleation of DRX grains. This twin-stimulated process accelerates continuous DRX through progressive lattice rotation and subgrain boundary migration. The resulting high-density grain boundaries not only enhance grain boundary sliding and rotation to accommodate large plastic strain, but also facilitate the transition from twinning-dominated deformation to non-basal slip activity once primary twins are exhausted. This ''twinning-assisted DRX''

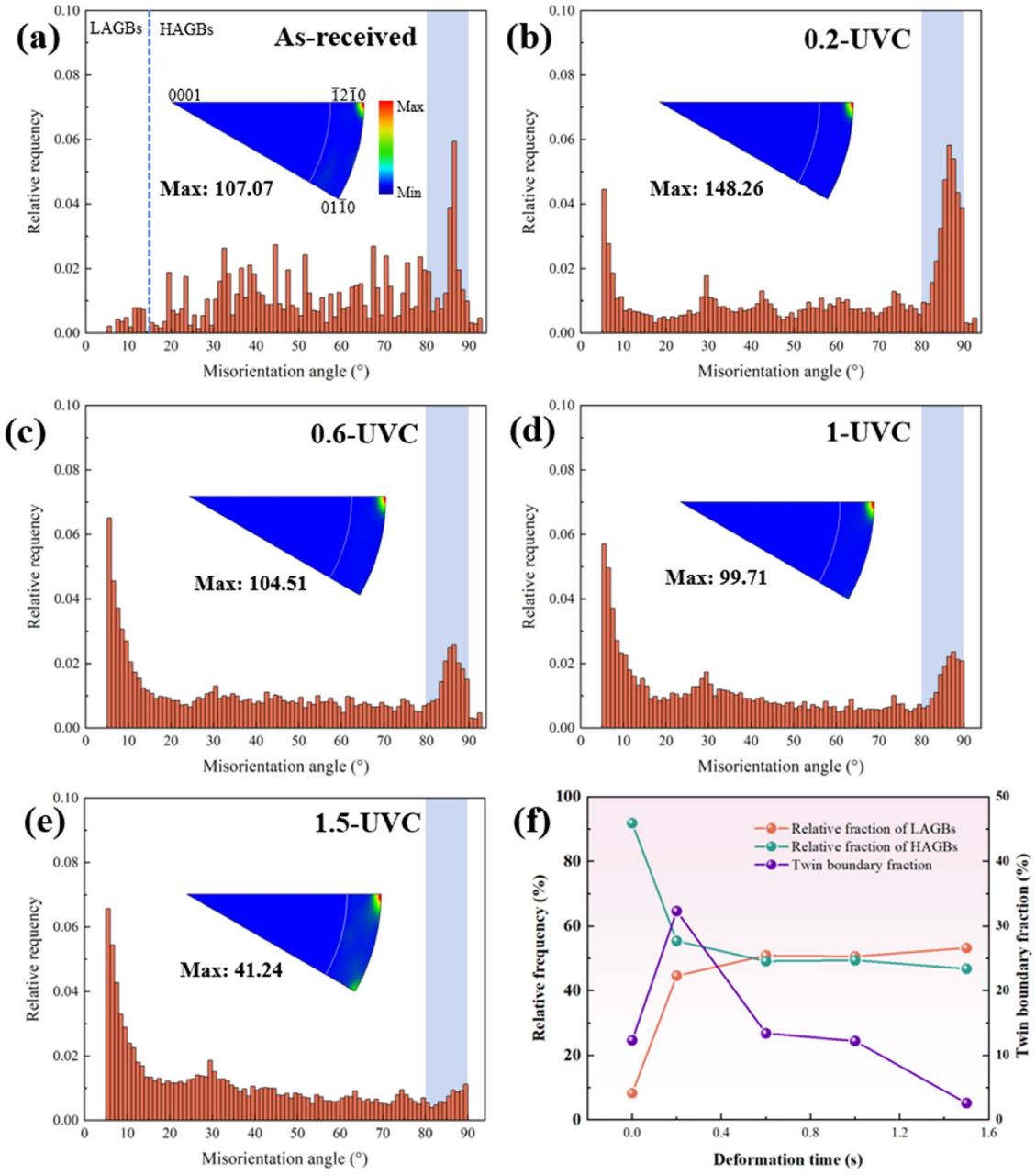

Fig. 8. Distributions of misorientation angle before and after UVC: (a) as-received alloy, (b) 0.2- UVC, (c) 0.6-UVC, (d) 1-UVC, (e) 1.5-UVC; (f) the curve of grain boundaries fraction and twin boundaries fraction with time.

mechanism is crucial for the early stages of deformation, as it locally softens the material and prevents stress concentrations from reaching critical levels that would otherwise induce fracture.

4.2.2. Dislocation proliferation and slip mode transition

In order to determine the specific dislocation slip modes activated during UVC, the widely established in-grain misorientation axis (IGMA) analysis was adopted. This methodology follows Chun et al. [65], where IGMA identifies activated slip modes by correlating the preferred lattice rotation axes (Taylor axes). Considering the crystal lattice bending caused by slip around Taylor axes, we adopted Mg alloy slip system criteria from Jiang et al. [66]. Misorientation axes were plotted for material-point pairs within 1.2°–2° range, as misorientation angles above 2° negligibly affect IGMA distribution features [67]. Fig. 10a–10d illustrates the resulting IGMA distributions for representative deformed grains, and grains with grain orientation spread (GOS) >1° was defined as deformed grains, following Huang et al. [68]. It is well known that the basal slip is easy to activate at room temperature. In Fig. 10a, the IGMA distribution of the B grain exhibits a concentration on the <0001> axis, indicating the activation of prismatic <a> slip. With the accumu-

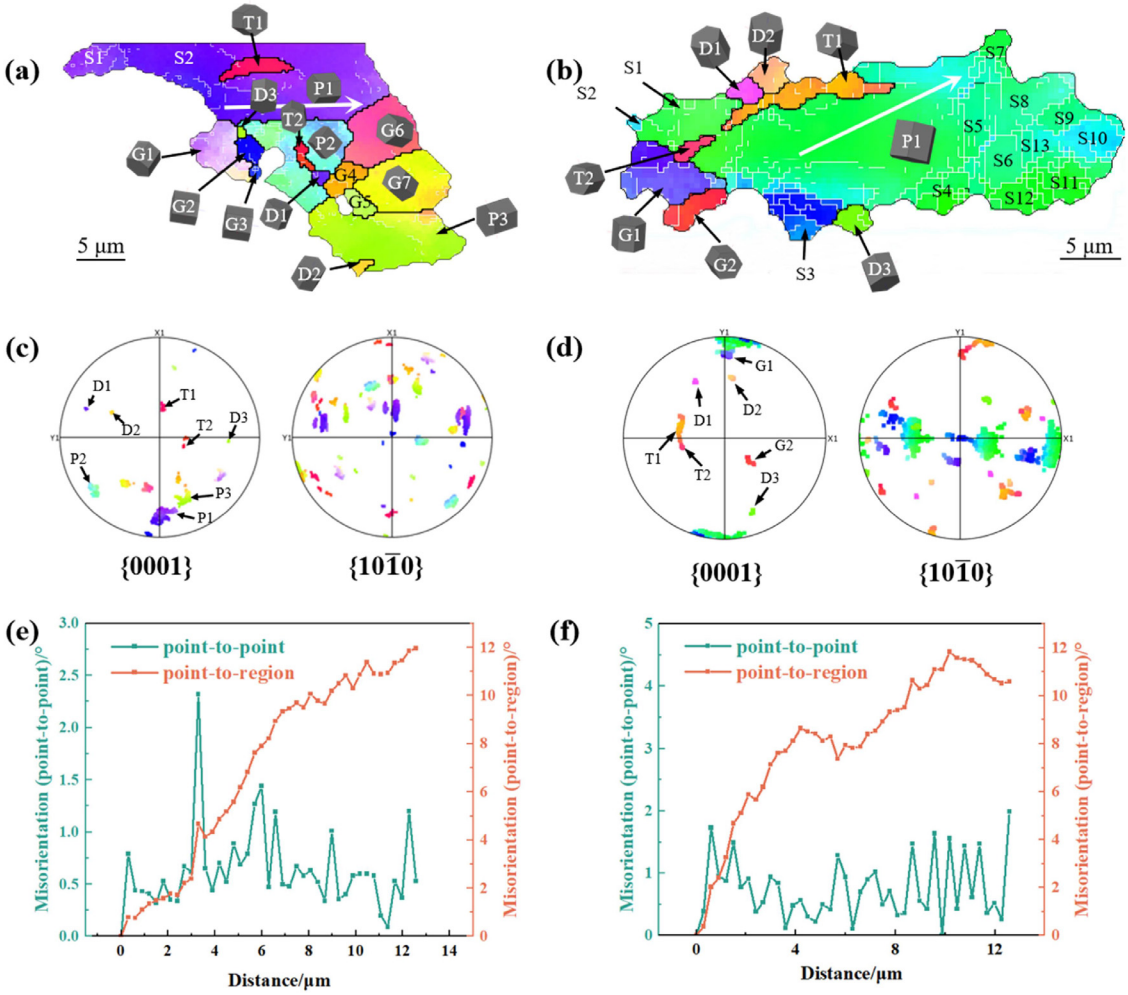

Fig. 9. Twin-induced nucleation behavior of 0.2-UVC and 0.6-UVC alloy: (a) region selected from Fig. 5b1 of 0.2-UVC alloy, (c) the corresponding {0001} {10-10} pole figures, (e) distributions of the misorientation angles along the white line in (a); (b) region selected from Fig. 5c1 of 0.6-UVC alloy, (d) the corresponding {0001} {10-10} pole figures, (f) distributions of the misorientation angles along the white line in (b).

lation of strain and the concomitant rise in temperature, the IGMA distributions are concentrated in the <uvt0> axis, indicating that the deformation of grains is mainly governed by the combined activity of basal <a> slip and pyramidal II <c + a> slip. In addition, the pyramidal II <c + a> slip leads to the grain rotation, activates the recrystallization, and increases the DRXed degree. With continuous increase in strain and a decrease in temperature, the prismatic <a> slip is activated (Fig. 10d). According to Qi et al. [69], prismatic <a> dislocations are more easily activated with a decreasing temperature. These observations indicate that the IGMA of most deformed grains is concentrated in the < uvt0 > axis.

Based on the above IGMA analyses, the deformation of the AZ31 alloy under UVC is dominated by basal <a> slip, working in concert with pyramidal II <c + a> slip. After the intermediate stage of deformation, the prismatic <a> slip dominates the deformation inside the grains.

Fig. 10e–h presents the GOS distribution maps and the proportion of DRXed grains. In the early stage of ultrasonic deformation, the proportion of DRXed grains changes dramatically, from 4.05% of the 0.2-UVC alloy to 12.5% of the 0.6-UVC alloy. Although most grains are still deformed grains, the proportion of DRXed grains in the 1.5-UVC alloy also reaches 15.45%. In addition, TEM observation was performed to determine the dominant slip mode. As shown in Fig. 11, a more comprehensive view of shear band morphology is achieved using FIB tomography (Fig. 11a). Fig. 11b–c further verifies the role of shear bands in the deformation process, and finer grains nucleate within the shear bands. Fig. 11d–e shows a high-resolution TEM (HR-TEM) image of the dislocations entangled region, and a one-dimensional inverse FFT image reveals dislocations associated with a different set of planes, marked by symbol ⊥. As shown in Fig. 11f, abundant dislocations could be observed, implying that <a> prismatic slips on (11–20) planes are activated. This slip mode plays a crucial role in accommodating the later plastic strain [70].

Fig. 12 shows the kernel average misorientation (KAM) analysis of the UVC alloys. The geometrically necessary dislocation (GND) density can be further calculated according

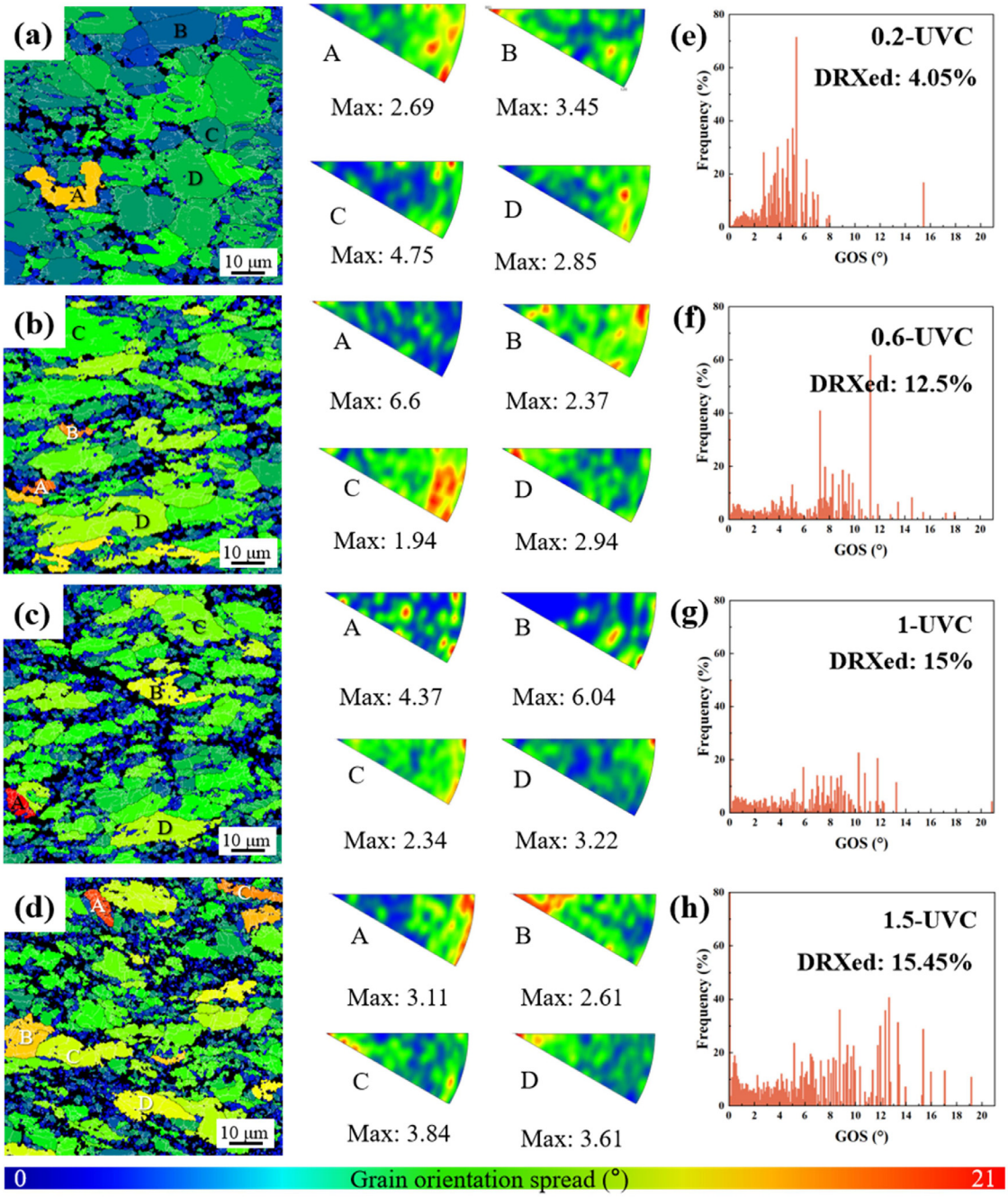

Fig. 10. GOS maps and IGMA distribution of AZ31-UVC alloy: (a) 0.2-UVC alloy, (b) 0.6-UVC alloy, (c) 1-UVC alloy, (d) 1.5-UVC alloy, (e-h) GOS distributions and the proportion of DRXed grains.

to the KAM value [71,72], which can be determined as:

$$\rho = \frac{2\theta}{\mu b} \tag{3}$$

Where θ (*rad*) can be calculated from the average KAM value from Fig. 12f; μ represents the step size of the EBSD observation, which is 0.3 μm in this work; b is the Burgers vectors of the basal slip of Mg at about 0.321 nm.

The GND densities of the as-received, 0.2-UVC, 0.6-UVC, 1-UVC, and 1.5-UVC alloys are calculated by EBSD as $1.16 \times 10^{14}/m^2$, $3.37 \times 10^{14}/m^2$, $3.59 \times 10^{14}/m^2$, $4.35 \times 10^{14}/m^2$ and $3.41 \times 10^{14}/m^2$, respectively. With increasing deformation time, the average GND densitiy first increases and then decreases. In the 0.2-UVC alloy, the dislocation is mainly concentrated at the grain boundary. When the deformation time reaches 0.6 s, the proportion of dislocations in the coarse grains is higher with the entanglement of dislocations. The maximum GND densities reaches $4.35 \times 10^{14}/m^2$ in the 1-UVC alloy. The results indicate that the formation of DRX is promoted in the deformation process, which reduces the dislocation density in the deformed structure. Recrystallized grains are generally dislocation-free, in-

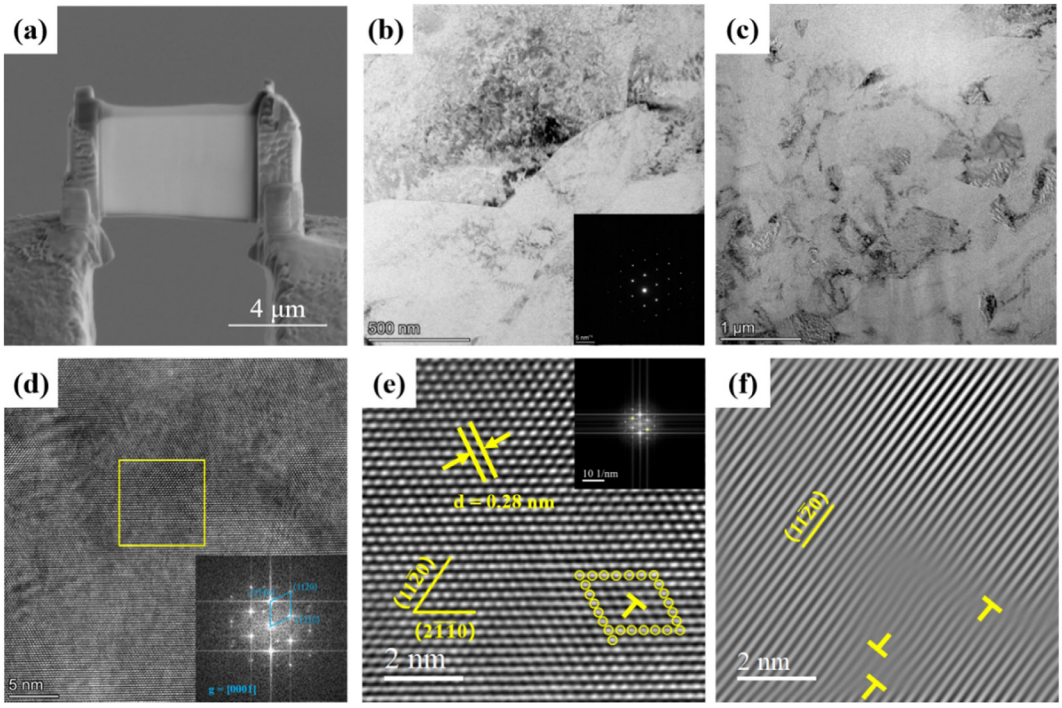

Fig. 11. HR-TEM showing typical dislocation area fringes of 1.5-UVC alloy: (a) FIB image during slicing. (b) (c) The TEM image inside the shear bands; (d) The HRTEM diagram shows the arrangement of atoms of the dislocation-rich region A, (e) enlarged squared area of (d); (f) one-dimensional Fourier-filtered image of (d).

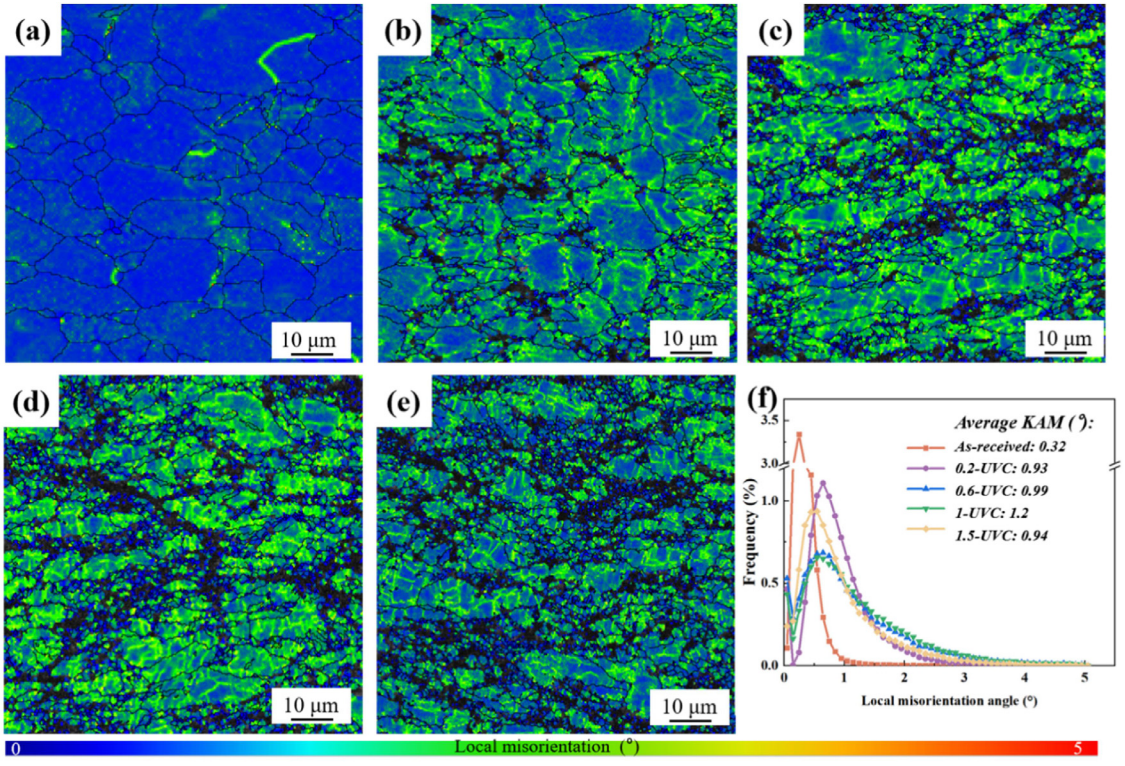

Fig. 12. Kernel average misorientation (KAM) distribution maps of AZ31 alloy before and after UVC. (a) As-received alloy, (b) 0.2-UVC alloy, (c) 0.6-UVC alloy, (d) 1-UVC alloy, (e) 1.5-UVC alloy, (f) corresponding statistical distribution image of KAM.

dicating that DRX can still occur at a temperature lower than the recrystallization temperature in this work. In the intermediate and advanced stages of deformation, the shear bands gradually pass through the interior of the sample section at 45° with a higher proportion. Shear bands are generally considered as defects that occur after severe plastic deformation [73].

However, Hu et al. [74] have reported that shear bands can sustain high-speed deformation of the alloy. In this work, shear bands similarly serve as a driving force for plasticity. Consequently, a large number of low-density, refined grains are generated around the shear bands, acting as reliable nucleation sites. Meanwhile, the overall dislocation density declines, indicating that shear bands coordinate deformation by enabling dislocation slip to keep pace with the rapid deformation rate induced by ultrasonic vibration.

The initial rapid increase in dislocation density reflects the intense acoustic impacts and high-frequency cyclic loading, which generate abundant mobile dislocations and stored energy far exceeding conventional compression. This high dislocation activity drives profuse twinning and shear-band formation in the early stage, while the subsequent decline in dislocation density coincides with the onset of twin-stimulated DRX. The recrystallized grains, being dislocation-free, provide soft regions that accommodate further strain, while the retained mobile dislocations in the matrix facilitate the transition to non-basal slip systems (prismatic and pyramidal <c + a> slip) once primary twins are exhausted. The shear bands acting as localized high-plasticity channels, coordinate the dislocation glide and grain boundary sliding [75], effectively releasing stress concentrations and suppressing crack initiation even at a high strain rate of 0.3 s^{-1}.

4.2.3. DRX evolution and grain refinement

To further explore the DRX mechanism during the high strain deformation stage, the deformation areas of 1.5-UVC alloy were analyzed in detail, as shown in Fig. 13. The band contrast (BC) and IPF maps (Fig. 13a–b) reveal coarse deformed grains coexist with fine recrystallized grains clustered along the shear bands, with average grain size (AGS) of 1.76 μm. The corresponding KAM map (Fig. 13c) confirms that a high density of dislocations is accumulated within these deformed zones. To resolve the fine substructures, TKD analysis focused on the shear band region (Region A) is presented in Fig. 13d, which reveals that inside the shear bands had more ultrafine grains with an average size of 0.48 μm. Fig. 13e represents the misorientation angle distributed along line 1 in Fig. 13c. Through the point-to-point angle, it can be found that there are several LAGBs along the line 1, and the point-to-region angle has accumulated up to about 35°, indicating the activation of extensive dislocation slips in the shear bands. In contrast to the gradual lattice rotation observed in Line 1, the misorientation profiles along Line 2 (Fig. 13f) and Line 3 (Fig. 13g) exhibit distinct characteristics of fully recrystallized grains. Notably, the point-to-region misorientation exhibits a ''step-like'' trend with flat plateaus within the grains. This implies that the interior of these DRX grains is relatively uniform in orientation and free of lattice distortion, confirming that the stored strain energy has been effectively released through recrystallization. The results above align well with the ''shear band induced nucleation'' mechanism recently reported by Zhang et al., who confirmed that shear bands act as preferential sites for DRX [76].

The severe accumulation of dislocations and lattice distortion provides the thermodynamic driving force for nucleation. Yet, the presence of these defects alone does not explain the suppression of fracture, given that similar features often cause failure during conventional compression [77]. This distinction points to a unique acoustic-thermal coupling mechanism inherent to the UVC process. Under 20 kHz ultrasonic vibration, the extremely high strain rate introduces massive stored energy into the shear bands [78], which is rapidly unlocked by intrinsic self-heating. Plastic work and internal friction dissipate as thermal energy, causing localized temperature spikes. Unlike conventional external heating, this ultrasonic-induced thermal field provides immediate kinetic activation for grain boundary migration directly at the sites of severe deformation. Thus, the formation of ultrafine grains results from a synergy: the stored energy lowers the nucleation barrier, while concurrent self-heating supplies the kinetics necessary for rapid DRX, significantly accelerating recrystallization compared to conventional deformation.

4.3. The reasons for AZ31 alloy to achieve super malleability without fracture during UVC process

4.3.1. The reasons for high-strain-rate super malleability

In this work, the role of dynamic impact from ultrasonic in inducing greater plastic deformation in AZ31 alloy cannot be ignored [79]. During deformation, the ultrasonic sonotrode carried out reciprocating loading and unloading at a set frequency and amplitude, causing separation and micro-sliding between the sonotrode and the sample surface [80]. Local friction at the contact interface generated heat, raising the local temperature. Therefore, the maximum instantaneous temperature of the internal heating of the AZ31 alloy can reach 478 K (Fig. 3) due to the thermal effect of ultrasound, which further reduced the yield stress and increased the surface plastic strain. In addition to the surface effects of UVC, acoustic softening is also considered to impact the microstructure evolution. Generally, acoustic softening is understood to facilitate dislocation motion and reduce the lattice resistance to dislocations, consequently manifests as a drop in flow stress [81]. Due to the rapid action of ultrasonic energy in a few milliseconds, the dislocation density increased and plied up significantly in the early stage of deformation. In order to release strain energy, dislocations reconstituted into dislocation walls, forming substructures oriented along the inclined direction relative to the ultrasonic vibration direction (Fig. 6k). In response to rapid deformation, shear bands formed to absorb the ultrasonic energy, accommodating a large number of dislocations and substructures. As the strain increased and the thermal effect diminished, DRX occurred within and around the shear bands [82].

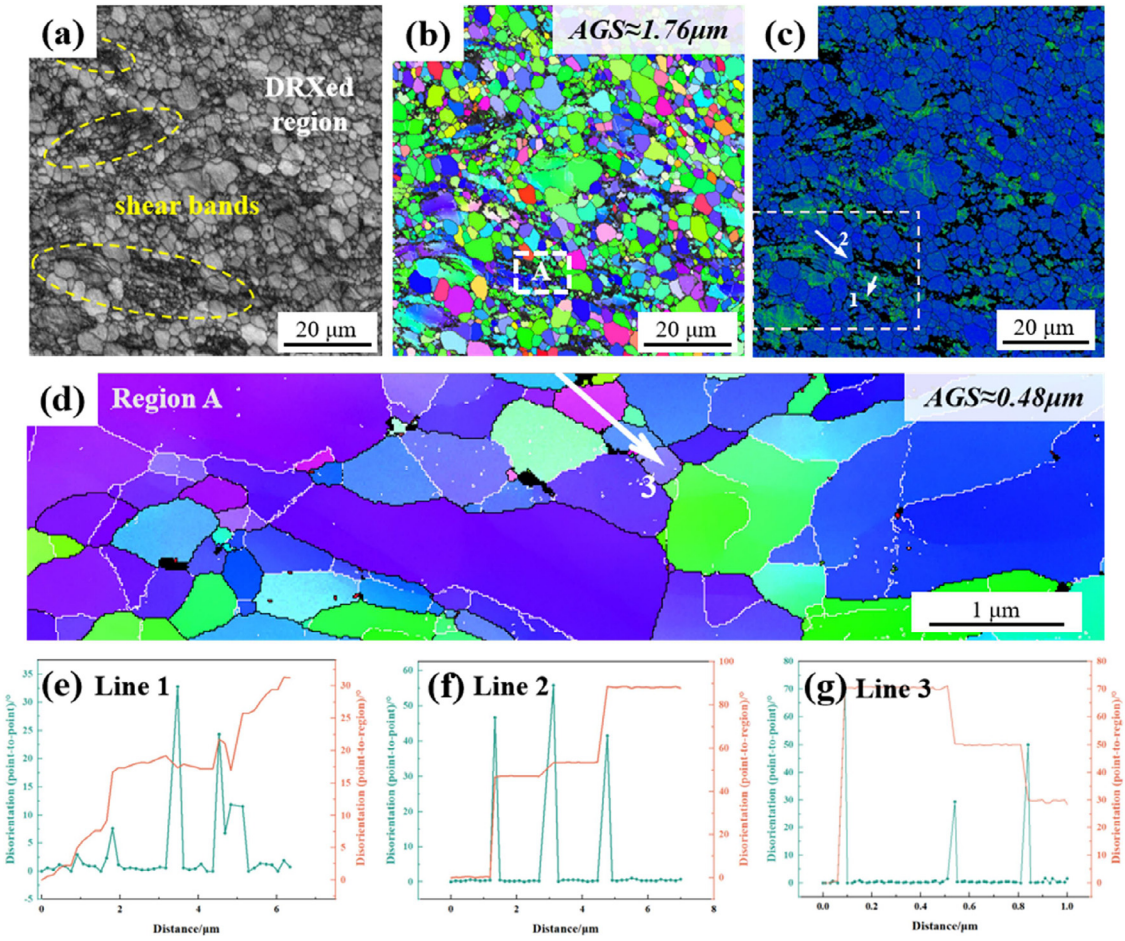

Fig. 13. EBSD analysis of 1.5-UVC alloy. (a) BC map, (b) IPF map, (c) KAM map; (d) TKD orientation map and IPF map of region A in Fig. 13b, (e) (f) (g) misorientation profiles of selected lines.

The combined acoustic softening and surface effects of ultrasonic vibration promote the plastic deformation of Mg alloy, with strain increasing nearly linearly. During low-strain UVC, twinning can be activated to accommodate sample deformation. These twins can then stimulate DRX and promote the formation of sub-grains afterward. Unlike conventional unidirectional loading, ultrasonic vibration loading provides multi-directional stress that induces severe lattice rotation, facilitating dislocations accommodation and stress concentration release during the transition of sub-grain boundaries to DRX. With the increase of true strain, the density of shear bands and dislocations increases, and the temperature of the sample reaches the maximum. The twins within the coarse grains provide nucleation points for recrystallization, while the entangled dislocations within the shear bands increase gradually. This is due to the ultrasonic vibration energy is absorbed by the dislocations in the shear band, which promotes the accumulation and entanglement of dislocations. With grain refinement, primary twins are exhausted, and non-basal slip is activated to dominate the deformation behavior. It is reasonable to speculate that ultrasonic energy is not fully absorbed due to heat dissipation. Dislocation slips dominated deformation as deformation continues and temperature decreases. With increasing the true strain, the density and distribution of shear bands increase correspondingly. Dislocations within shear bands develop into sub-grain, and DRX occurs simultaneously around and within shear band regions, coordinating deformation. According to Zohrevand et al. [83], ultrasonic waves can induce sufficient shear stress to wipe out twins and promote the accumulation of dislocations and non-basal slips. Most of the grains inside and around shear bands recrystallized, eventually realizing a uniform structure mainly responsible for the obtained super malleability. This discussion provides new insights into the underlying mechanisms of the ultrasonic process.

4.3.2. The reasons for super malleability without fracture

Generally speaking, nucleation and development of microcracks and fracture of Mg alloys during compression originate at twin boundaries, eutectic particles, and grain boundaries [84]. Malik et al. [85] reported the deformation behavior of ZK61 alloy under conventional compression at different temperatures. A large number of compression twins were produced under ambient conditions without external heating while DRX is difficult to be initiated. The fraction of twinning increased along with increasing strain rate. Twinning

produced high strain energy contributing to work hardening, while limiting further plastic deformation. Stress concentration at twin and grain boundaries is the primary cause for crack nucleation and propagation. Kim et al. [86] observed that DRX caused by compression twins in the shear bands can accommodate large plastic strain. The initiation of cracks can be induced by strain incompatibility between high strain energy regions and the matrix structure. Lu et al. [87] reported asymmetric deformation among grains during compression resulting from stress concentration at the boundaries of elongated grains.

In the present study, the AZ31 alloy exhibited no fracture under large-strain UVC processing. This super-malleability can be attributed to unique microstructural evolution driven by ultrasonic energy. Firstly, during the early stage of UVC, twinning accommodated deformation and provided initial nucleation sites for DRX. As true strain increased from 0.2 to 0.6, twinning was effectively exhausted, mitigating the potential for twin-induced cracking by ultrasonic softening. Secondly, to accommodate high-frequency ultrasonic vibration, a large number of dislocations were generated and clustered into shear bands along the maximum shear direction. Under the acoustic softening effect, dislocation multiplication was enhanced, and the density of shear bands increased, improving the material's capacity to accommodate severe deformation.

Crucially, ultrafine grains formed via DRX within these shear bands play a pivotal role in achieving super-malleability. In conventional deformation, shear bands often act as failure precursors due to severe stress concentration [88]. However, under UVC, rapid formation of newly formed ultrafine grains effectively releases these local stress concentrations and induces localized dynamic softening. Furthermore, abundant high-angle grain boundaries provided by these ultrafine grains facilitated grain boundary sliding and coordinated rotation. This mechanism effectively prevents crack initiation at shear bands, enabling the material to sustain an exceptionally large true strain of 1.7 without fracture.

4.4. Potential applications and limitations

Although UVC demonstrates remarkable capability for achieving super-malleability in Mg alloys under room-temperature conditions, its translation from laboratory-scale to industrial implementation requires balanced evaluation of both advantages and limitations.

Currently, the UVC system is primarily optimized for precision components with characteristic dimensions up to approximately 30 mm, making it particularly suitable for small-scale, high-value products, such as biomedical implants, aerospace fasteners, and micro-gears. Scaling the process to larger structural components (>100 mm) faces challenges associated with the power capacity of ultrasonic transducers and the acoustic design and durability of large-section sonotrodes. Despite these challenges, UVC offers distinct advantages in processing efficiency and cost-effectiveness. Unlike conventional superplastic forming requiring prolonged high-temperature exposure, UVC operates without external heating and completes forming within seconds. This significantly reduces energy consumption per component and increases production throughput. Moreover, the elimination of mold preheating alleviates thermal fatigue, thereby extending the service life of forming dies. As a result, for mass production of complex near-net-shape Mg components, the reduced operational costs associated with UVC can partially or even fully compensate for higher initial capital expenditures.

Another commonly cited concern for ultrasonic-based processing is energy attenuation. In contrast to the pronounced attenuation observed in liquid or gaseous media, UVC relies on direct solid-state mechanical coupling between the sonotrode and the workpiece. When the acoustic system is properly tuned to resonance, high-frequency mechanical energy can be efficiently transmitted with minimal loss during the forming process [89].

In summary, the UVC represents a promising and potentially transformative approach for high-efficiency manufacturing of precision Mg components. Further systematic studies on process stability, tooling lifetime, and scale-up design are still required before large-scale industrial deployment. Continued advances in high-power acoustic systems and sonotrode design are expected to further extend its applicability toward larger critical components in emerging fields, including lightweight structural nodes for robotics, unmanned aerial vehicles, and automotive systems.

5. Conclusions

In summary, an effective approach of ultrasonic vibration-assisted compression to realize the super malleability on the commercial AZ31 alloy sheet initiated at room temperature is successfully developed in this study. The dominating deformation mechanisms enabling the super malleability are dissected by characterizing the microstructure evolutions with different periods of processing. Based on the experimental results, the main conclusions can be drawn as follows:

(1) High strain rate (3×10^{-1} s^{-1}) super malleability is successfully achieved in an AZ31 alloy sheet by UVC initiated at room temperature with a relatively low applied stress (~43.23 MPa). A true strain of nearly 1.7 and circumference expansion of 140% are obtained just within 2 s. This demonstrates UVC's capability for near-room-temperature forming of Mg products with various complex geometries.
(2) The microstructure evolution during the UVC process goes through three distinct stages. In the initial stage, the deformation is coordinated primarily by twinning and twin-induced DRX. Subsequently, as primary twins are exhausted, a transition to non-basal slip dominance occurs. In the final stage, deformation is governed by the formation of high-density shear bands and widespread DRX, ensuring continuous strain accommodation from low to high strain levels.
(3) The achieved super-malleability is attributed to a synergistic acoustic-thermal coupling mechanism. The ultrasonic-induced acoustic softening and localized self-heating sig-

nificantly lower the nucleation barrier, activating rapid DRX within the shear bands. The ultrafine grains (~460 nm) were rapidly generated within the shear bands. The formation of a large number of new grain boundaries and the homogenization of the microstructure release stress concentration, preventing fracture. This technique provides a simple and effective approach to develop Mg alloy products at room temperature with significant industrial applicability.

Data availability

The raw/processed data required to reproduce these findings are available from the corresponding author by request.

Declaration of competing interest

Jinghua Jiang is an editorial board member for Journal of Magnesium and Alloys and was not involved in the editorial review or the decision to publish this article. All authors declare that there are no competing interests.

CRediT authorship contribution statement

Ziyue Xu: Writing – original draft, Methodology, Investigation. **Huan Liu:** Writing – review & editing, Supervision, Resources, Conceptualization. **Chao Sun:** Methodology, Investigation, Data curation. **Luyao Li:** Resources, Methodology. **Yuna Wu:** Visualization, Validation. **Yue Zhang:** Visualization, Validation, Software. **Jinghua Jiang:** Visualization, Formal analysis, Data curation. **Jing Bai:** Software, Resources, Methodology. **Yunchang Xin:** Writing – review & editing, Software, Conceptualization. **Jiang Ma:** Writing – review & editing, Resources, Conceptualization.

Acknowledgements

This work was supported by the National Natural Science Foundation of China (52271101, 52571137), Basic Research Program of Jiangsu (BK20243005 and BK20232025), the Nanjing Major Science and Technology Project (202309015), and the Suzhou Science and Technology Project (SYG202312, SJC2023005, SZS2023023). The authors also thank the support from Jiangsu Provincial Engineering Research Center for Structure-Function Integrated Metallic Materials for Harsh Environments, and Innovation Center for Critical Materials in Hydraulic Infrastructure Safety and Water Environment Restoration of Hohai University.

Supplementary materials

Supplementary material associated with this article can be found, in the online version, at doi:10.1016/j.jma.2026.102094.

References

[1] G.G. Wang, J.P. Weiler, J. Magnes. Alloys 11 (2023) 78–87, doi:10.1016/j.jma.2022.10.001.
[2] F.Z. Akbarzadeh, M. Sarraf, E.R. Ghomi, V.V. Kumar, M. Salehi, S. Ramakrishna, S. Bae, J. Magnes. Alloys 12 (2024) 2569–2594, doi:10.1016/j.jma.2024.06.015.
[3] R. Roumina, S. Lee, T.D. Berman, K.S. Shanks, J.E. Allison, A. Bucsek, Acta Mater. 234 (2022) 118039, doi:10.1016/j.actamat.2022.118039.
[4] T. Nakata, S. Kamado, J. Magnes. Alloys 11 (2023) 3992–4010, doi:10.1016/j.jma.2023.08.006.
[5] B. Liu, J. Yang, X. Zhang, Q. Yang, J. Zhang, X. Li, J. Magnes. Alloys 11 (2023) 15–47, doi:10.1016/j.jma.2022.12.015.
[6] D.F. Shi, A. Ma, M.T. Perez-Prado, C.M. Cepeda-Jimenez, Acta Mater. 244 (2023) 118555, doi:10.1016/j.actamat.2022.118555.
[7] Z.J. Yu, Y.D. Huang, L.L. Liu, K. Shi, B.T. Du, K. Liu, S.B. Li, W.B. Du, Scr. Mater. 220 (2022) 114901, doi:10.1016/j.scriptamat.2022.114901.
[8] X. Zhang, J. Li, L. Wang, Y. Cheng, W. Lei, Q. Chen, J. Magnes. Alloys 13 (2025) 5243–5262, doi:10.1016/j.jma.2025.08.032.
[9] K. Ahn, H.J. Lee, J. Yoon, Mater. Sci. Eng. A 651 (2016) 1010–1017, doi:10.1016/j.msea.2015.11.055.
[10] Y.Q. Li, F. Li, F.W. Kang, H.Q. Du, Z.Y. Chen, J. Alloys Compd. 953 (2023) 170080, doi:10.1016/j.jallcom.2023.170080.
[11] L. Zhang, Q. Yuan, J. Tan, Q. Dong, H. Lv, F. Wang, A. Tang, J. Eckert, F. Pan, J. Magnes. Alloys 12 (2024) 4741–4767, doi:10.1016/j.jma.2024.12.008.
[12] H.F. Zhang, Y.T. Ding, R.M. Li, Y.B. Gao, J. Mater. Res. Technol. 28 (2024) 1841–1851, doi:10.1016/j.jmrt.2023.12.127.
[13] M. Yang, H.L. Jia, R. Jiang, X.L. Zhou, P.K. Ma, Z.G. Li, M. Zha, H.Y. Wang, J. Magnes. Alloys 13 (2025) 2120–2143, doi:10.1016/j.jma.2024.06.029.
[14] M. Zhang, L. Zhong, W. Ju, M. Huo, W. Xia, Y. Zhang, Z. Zeng, Q. Shi, Y. Wang, M. Zhou, J. Magnes. Alloys 13 (2025) 5745–5762, doi:10.1016/j.jma.2025.05.003.
[15] H.C. Pan, R. Kang, J.R. Li, H.B. Xie, Z.R. Zeng, Q.Y. Huang, C.L. Yang, Y.P. Ren, G.W. Qin, Acta Mater. 186 (2020) 278–290, doi:10.1016/j.actamat.2020.01.017.
[16] T. Fu, X.Y. Sun, C.C. Ge, D.S. Xie, J.R. Li, H.C. Pan, G.W. Qin, J Alloys Compd. 917 (2022) 165407, doi:10.1016/j.jallcom.2022.165407.
[17] J. Li, M. Huang, J. Hou, X. Wang, G. Xu, Y. Yang, N. Mo, Y. Shi, L. Zhang, W. Tang, J. Magnes. Alloys 13 (2025) 3673–3688, doi:10.1016/j.jma.2025.03.026.
[18] L. Tong, J. Jiang, G. Bi, Y. Li, T. Chen, X. Zhang, D. Fang, X. Ding, J. Magnes. Alloys (2026) 101965, doi:10.1016/j.jma.2025.101965.
[19] Y. Chen, H. Yan, D. Wang, R.S. Chen, Trans. Nonferrous Met. Soc. China 33 (2023) 728–742, doi:10.1016/S1003-6326(22)66141-7.
[20] M.N. Zhang, H.L. Jia, M. Zha, L. Zhao, Z.M. Hua, C. Wang, Y.P. Gao, H.Y. Wang, Mater. Res. Lett. 11 (2023) 781–788, doi:10.1080/21663831.2023.2237996.
[21] S. Kumar, M. Panchal, A.N. Gandi, L. Kaushik, S.H. Choi, J. Singh, J. Magnes. Alloys 13 (2025) 1815–1828, doi:10.1016/j.jma.2025.02.017.
[22] S.Y. Lyu, G.D. Li, R.X. Zheng, W.L. Xiao, Y.D. Huang, N. Hort, M.F. Chen, C.L. Ma, Mater. Sci. Eng. A 856 (2022) 143783, doi:10.1016/j.msea.2022.143783.
[23] B. Song, M. Wang, R.L. Shi, Z.W. Du, N. Guo, F. Wang, S.F. Guo, J. Magnes. Alloys 11 (2023) 2096–2105, doi:10.1016/j.jma.2021.08.012.
[24] J.J. He, Y. Mao, S.L. Lu, K. Xiong, S.M. Zhang, B. Jiang, F.S. Pan, Mater. Sci. Eng. A 760 (2019) 174–185, doi:10.1016/j.msea.2019.06.007.
[25] X. Liu, D.D. He, B.W. Zhu, W.H. Liu, F. Ye, F. Wei, C.C. Xu, L.X. Li, Scr. Mater. 253 (2024) 116296, doi:10.1016/j.scriptamat.2024.116296.
[26] H.W. Jiang, F. Li, X. Zeng, J. Mater. Sci. Technol 33 (2017) 573–579, doi:10.1016/j.jmst.2017.01.003.
[27] D. Xu, X. Liu, H. Wu, D. An, Q. Hu, X. Li, J. Chen, J. Magnes. Alloys 13 (2025) 5989–6000, doi:10.1016/j.jma.2024.11.006.
[28] H. Wu, J. Jiang, Z. Yang, M. Li, H. Huang, N. Ge, A. Ma, H. Liu, J. Magnes. Alloys 11 (2023) 3765–3778, doi:10.1016/j.jma.2022.03.003.

[29] H.R. Wu, J.H. Jiang, Z.Q. Yang, M.J. Li, H.J. Huang, N.F. Ge, A.B. Ma, H. Liu, J. Magnes. Alloys 11 (2023) 3765–3778, doi:10.1016/j.jma.2022.03.003.
[30] F. Lin, J. Li, H.W. Zhao, L.L. Sun, Z.T. Chen, Q.S. Meng, Mod. Phys. Lett. B 27 (2013) 1341022, doi:10.1142/S0217984913410224.
[31] F.D. Ning, W.L. Cong, J. Manuf. Process 51 (2020) 174–190, doi:10.1016/j.jmapro.2020.01.028.
[32] W.X. Xu, L.C. Zhang, Adv. Manuf. 3 (2015) 173–192, doi:10.1007/s40436-015-0115-4.
[33] R.R. Dehoff, S.S. Babu, Acta Mater. 58 (2010) 4305–4315, doi:10.1016/j.actamat.2010.03.006.
[34] Y.J. Hu, J.Y. Wang, W. Zhai, B. Wei, J. Magnes. Alloys 11 (2023) 3829–3839, doi:10.1016/j.jma.2023.08.015.
[35] S.S. Dash, R.C. Fernandes, X. Shang, Y. Zou, H. Peng, X. Jiang, X. Fang, N. Ma, D. Li, D. Chen, J. Magnes. Alloys 13 (2025) 1939–1952, doi:10.1016/j.jma.2025.03.005.
[36] J.C. Hung, Y.P. Tsai, C.H. Hung, Precis. Eng. 37 (2013) 222–227, doi:10.1016/j.precisioneng.2012.06.002.
[37] C. Bunget, G. Ngaile, Ultrasonics 51 (2011) 606–616, doi:10.1016/j.ultras.2011.01.001.
[38] M. Murakawa, M. Jin, J. Mater. Process Technol. 113 (2001) 81–86, doi:10.1016/S0924-0136(01)00635-5.
[39] Y. Fan, Z. Liu, Z. Hao, Precis. Eng. 99 (2026) 45–56, doi:10.1016/j.precisioneng.2026.01.005.
[40] B. An, J. Li, Z. Li, D. Wu, R. Li, Mech. Mater. 212 (2026) 105539, doi:10.1016/j.mechmat.2025.105539.
[41] W.X. Wen, L.Y. Li, Z. Li, W.Q. Ruan, S. Ren, Z.X. Zhang, X. Liang, H. Liu, J. Ma, Rare Met. 42 (2023) 1146–1153, doi:10.1007/s12598-022-02171-2.
[42] L.Y. Li, G.J. Lyu, H.Z. Li, C.T. Fan, W.X. Wen, H.J. Lin, B. Huang, S. Sohrabi, S. Ren, X. Liang, Y.J. Wang, J. Ma, W.H. Wang, J. Mater. Sci. Technol. 142 (2023) 76–88, doi:10.1016/j.jmst.2022.09.028.
[43] L.Y. Li, J.Y. Chen, L.X. Zhu, Y. Zhang, J. Zhu, X. Li, W. Li, K.Y. Lin, X.R. Zhao, X.D. Liu, C.C. Yuan, J. Ma, Rare Met. (2025), doi:10.1007/s12598-025-03603-5.
[44] J. Ma, X. Liang, X.Y. Wu, Z.Y. Liu, Sci. Rep. 5 (2015) 17844, doi:10.1038/srep17844.
[45] Y. Zhang, P. Huang, L. Li, X. Li, W. Wen, S. Sohrabi, J. Huang, W. Lu, Y. Xiao, D. Li, J. Ma, J. Manuf. Process 139 (2025) 12–24, doi:10.1016/j.jmapro.2025.01.097.
[46] R.X. Li, X. Li, J. Ma, Y. Zhang, Intermetallics 121 (2020) 106780, doi:10.1016/j.intermet.2020.106780.
[47] Y. Lou, Y. Lingyun, S.P. Xv, J. Ma, Intermetallics 142 (2022) 107467, doi:10.1016/j.intermet.2022.107467.
[48] L.Y. Li, X. Li, Z.Y. Huang, J.B. Huang, Z.H. Liu, J.N. Fu, W.X. Wen, Y. Zhang, S.K. Huang, S. Ren, J. Ma, Nat. Commun. 14 (2023) 6305, doi:10.1038/s41467-023-42014-x.
[49] J. Ma, C. Yang, X.D. Liu, B.S. Shang, Q.F. He, F.C. Li, T.Y. Wang, D. Wei, X. Liang, X.Y. Wu, Y.J. Wang, F. Gong, P.F. Guan, W.H. Wang, Y. Yang, Sci. Adv. 5 (2019) eaax7256, doi:10.1126/sciadv.aax7256.
[50] L.Y. Li, W.X. Wen, J.A. Fu, J. Ma, Intermetallics 149 (2022) 107672, doi:10.1016/j.intermet.2022.107672.
[51] M. Li, X. Wang, Y. Liu, Z.B. Xiao, Y.C. Huang, J. Alloys Compd. 947 (2023) 169523, doi:10.1016/j.jallcom.2023.169523.
[52] X.J. Zhu, Q.B. Fan, D.D. Wang, H.C. Gong, Y. Gao, F. Qian, S.B. Jin, G. Sha, Scr. Mater. 206 (2022) 114229, doi:10.1016/j.scriptamat.2021.114229.
[53] X.J. Liu, T.H. Le, S. Yuan, J.H. Wang, W.L. Cheng, X.Q. Li, P.P. Jin, J. Mater. Res. Technol. 23 (2023) 4293–4306, doi:10.1016/j.jmrt.2023.02.047.
[54] Y.W. Gui, L.X. Ouyang, Y.J. Cui, H.K. Bian, Q.A. Li, A. Chiba, J. Magnes. Alloys 9 (2021) 456–466, doi:10.1016/j.jma.2020.06.001.
[55] H.L. Kim, J.H. Lee, C.S. Lee, W. Bang, S.H. Ahn, Y.W. Chang, Mater. Sci. Eng. A 558 (2012) 431–438, doi:10.1016/j.msea.2012.08.023.
[56] D.F. Lou, M.D. Zhang, J.Z. Lv, B.X. Li, X.W. Wang, J.H. Shi, Y.P. Ren, H.X. Li, G.W. Qin, J. Alloys Compd. 896 (2022) 162912, doi:10.1016/j.jallcom.2021.162912.
[57] D.F. Shi, A. Ma, M.T. Pérez-Prado, C.-Jé CM, Acta Mater. 244 (2023) 118555, doi:10.1016/j.actamat.2022.118555.
[58] D.K. Guan, W.M. Rainforth, J.H. Gao, L. Ma, B. Wynne, Acta Mater. 145 (2018) 399–412, doi:10.1016/j.actamat.2017.12.019.
[59] S. Wang, H. Pan, Z. Zeng, Z. Pan, S. Wang, D. Zhou, Z. Zeng, G. Qin, J. Magnes. Alloys 13 (2025) 5115–5131, doi:10.1016/j.jma.2025.07.016.
[60] Y.P. Li, Y.J. Cui, H.K. Bian, S.H. Sun, N. Tang, Y. Chen, B. Liu, Y. Koizumi, A. Chiba, Sci. Technol. Adv. Mater. 15 (2014) 035003, doi:10.1088/1468-6996/15/3/035003.
[61] D. Pei, L. Wang, X.H. Hu, X.L. Li, X. Wang, J. Mater. Sci. 58 (2023) 15529–15541, doi:10.1007/s10853-023-08990-7.
[62] S.W. Xu, S. Kamado, T. Honma, Scr. Mater. 63 (2010) 293–296, doi:10.1016/j.scriptamat.2010.04.012.
[63] B.Y. Lin, H. Zhang, Y.P. Meng, L.F. Wang, J.F. Fan, S.Z. Zhang, H.J. Roven, Mater. Sci. Eng. A 847 (2022) 143338, doi:10.1016/j.msea.2022.143338.
[64] Q. Ma, B. Li, E.B. Marin, S.J. Horstemeyer, Scr. Mater. 65 (2011) 823–826, doi:10.1016/j.scriptamat.2011.07.046.
[65] Y.B. Chun, M. Battaini, C.H.J. Davies, S.K. Hwang, Metall. Mater. Trans. A 41 (2010) 3473–3487, doi:10.1007/s11661-010-0410-4.
[66] Z.W. Jiang, D.D. Yin, Y.F. Wan, R. Ni, H. Zhou, J. Zheng, Q.D. Wang, Trans. Nonferrous Met. Soc. China 33 (2023) 79–94, doi:10.1016/S1003-6326(22)66092-8.
[67] D.Q. Ma, S.A. Yuan, S.Y. Luan, P.P. Jin, H.R. Hu, J.H. Wang, X.Q. Li, J. Mater. Res. Technol. 21 (2022) 1643–1654, doi:10.1016/j.jmrt.2022.10.012.
[68] X.D. Huang, Y.C. Xin, Y. Cao, W. Li, G.J. Huang, X. Zhao, Q. Liu, P.D. Wu, Int. J. Plast. 158 (2022) 103412, doi:10.1016/j.ijplas.2022.103412.
[69] X.X. Qi, Y.X. Li, X.Q. Zeng, J. Alloys Compd. 960 (2023) 170803, doi:10.1016/j.jallcom.2023.170803.
[70] B.L. Wu, L.H. Song, G. Wan, X.H. Du, J. Muller, C. Esling, J. Mater. Eng. Perform 29 (2020) 8145–8155, doi:10.1007/s11665-020-05279-7.
[71] C. Sun, H. Liu, Z.Y. Xu, Y.N. Wu, Y. Kai, J. Ju, J.H. Jiang, F. Xue, J. Bai, Y.C. Xin, J. Mater. Sci. Technol. 176 (2024) 13–24, doi:10.1016/j.jmst.2023.07.051.
[72] M.Y. Zhang, Y.Q. Zhang, H. Yu, H.X. Wang, X.F. Niu, L.F. Wang, H. Li, W.L. Cheng, Mater. Sci. Eng. A 853 (2022) 143788, doi:10.1016/j.msea.2022.143788.
[73] J.Y. Jiang, F. Jiang, M.H. Zhang, Z.Q. Tang, M.M. Tong, Mater. Charact. 175 (2021) 111081, doi:10.1016/j.matchar.2021.111081.
[74] X.X. Hu, N.H. Liu, V. Jambur, S. Attarian, R.R. Su, H.L. Zhang, J.Q. Xi, J. Perepezko, I. Szlufarska, Nat. Mater. 22 (2023) 1071–1077, doi:10.1038/s41563-023-01597-y.
[75] X. Liu, H. Yang, B.W. Zhu, Y.Z. Wu, W.H. Liu, C.P. Tang, J. Magnes. Alloys 10 (2022) 1096–1108, doi:10.1016/j.jma.2021.07.030.
[76] M.Q. Zhang, T. Nakata, C. Xu, G.Z. Tang, K.K. Deng, X.J. Wang, G.S. Wang, S. Kamado, L. Geng, J. Magnes. Alloys 13 (2025) 5525–5537, doi:10.1016/j.jma.2024.06.010.
[77] A. Malik, Y. Wang, C. Huanwu, F. Nazeer, B. Ahmed, M.A. Khan, W. Mingjun, Mater. Sci. Eng. A 771 (2020) 138649, doi:10.1016/j.msea.2019.138649.
[78] J. Han, J. Sun, Y. Song, B. Xu, Z. Yang, S. Xu, Y. Han, G. Wu, J. Zhao, J. Magnes. Alloys 11 (2023) 2392–2403, doi:10.1016/j.jma.2021.09.021.
[79] C. Li, X.F. Tang, H.D. Zhang, X.Y. Wang, L. Deng, M. Zhang, P. Gong, J.S. Jin, J. Alloys Compd. 913 (2022) 165238, doi:10.1016/j.jallcom.2022.165238.
[80] C. Shao, Z.L. Wang, J. Li, Y.D. Zhai, J. Lin, R.Q. Bai, Y.J. Guan, G.Q. Zhao, J. Mater. Res. Technol. 23 (2023) 2467–2478, doi:10.1016/j.jmrt.2023.01.185.
[81] J. Hu, T. Shimizu, M. Yang, Ultrason. Sonochem. 48 (2018) 240–248, doi:10.1016/j.ultsonch.2018.05.039.
[82] R. Pei, F.Z. Mouhib, M. Seehaus, S. Arnoldi, P.L. Sun, T. Al-Samman, J. Magnes. Alloys 13 (2025) 1088–1098, doi:10.1016/j.jma.2025.02.013.
[83] M. Zohrevand, M. Aghaie-Khafri, F. Forouzan, E. Vuorinen, Ultrasonics 116 (2021) 106519, doi:10.1016/j.ultras.2021.106519.
[84] S. Anbuselvan, S. Ramanathan, Mater. Des. 31 (2010) 2319–2323, doi:10.1016/j.matdes.2009.12.009.

[85] A. Malik, Y.W. Wang, C.H. Wu, F. Nazeer, B. Ahmed, M.A. Khan, W. Mingjun, Mater. Sci. Eng. A 771 (2020) 138649, doi:10.1016/j.msea.2019.138649.
[86] Y.J. Kim, Y.M. Kim, S.G. Hong, D.W. Kim, C.S. Lee, S.H. Park, J. Mater. Sci. Technol. 93 (2021) 41–52, doi:10.1016/j.jmst.2021.03.039.
[87] L.W. Lu, T.M. Liu, Y. Chen, Z.C. Wang, Mater. Charact. 67 (2012) 93–100, doi:10.1016/j.matchar.2012.02.023.
[88] J.L. Sun, P.W. Trimby, F.K. Yan, X.Z. Liao, N.R. Tao, J.T. Wang, Acta Mater. 79 (2014) 47–58, doi:10.1016/j.actamat.2014.07.011.
[89] J. Chen, S. Ren, Z. Chen, J. Dong, Z. Lu, J. Zhu, L. Zhu, Y. Zhan, X. Zhao, W. Wang, S. Zeng, J. Xiao, S. Sohrabi, X. Liang, K. Yang, D. Ma, J. Ma, Mater. Futures 4 (2025) 035003, doi:10.1088/2752-5724/adeeae.